

A Submillimeter Perspective on the GOODS Fields (SUPER GOODS). IV. The Submillimeter Properties of X-ray Sources in the CDF-S

A. J. BARGER,^{1,2,3} L. L. COWIE,³ F. E. BAUER,^{4,5,6} AND J. GONZÁLEZ-LÓPEZ^{7,8}

¹*Department of Astronomy, University of Wisconsin-Madison, 475 N. Charter Street, Madison, WI 53706, USA*

²*Department of Physics and Astronomy, University of Hawaii, 2505 Correa Road, Honolulu, HI 96822, USA*

³*Institute for Astronomy, University of Hawaii, 2680 Woodlawn Drive, Honolulu, HI 96822, USA*

⁴*Instituto de Astrofísica and Centro de Astroingeniería, Facultad de Física, Pontificia Universidad Católica de Chile, Casilla 306, Santiago 22, Chile*

⁵*Millennium Institute of Astrophysics (MAS), Nuncio Monseñor Sótero Sanz 100, Providencia, Santiago, Chile*

⁶*Space Science Institute, 4750 Walnut Street, Suite 205, Boulder, Colorado 80301, USA*

⁷*Núcleo de Astronomía de la Facultad de Ingeniería y Ciencias, Universidad Diego Portales, Av. Ejército Libertador 441, Santiago, Chile*

⁸*Instituto de Astrofísica and Centro de Astroingeniería, Facultad de Física, Pontificia Universidad Católica de Chile Casilla 306, Santiago 22, Chile*

ABSTRACT

The CDF-S is the deepest X-ray image available and will remain so for the near future. We provide a spectroscopic (64.5%; 64% with spectral classifications) and photometric redshift catalog for the full 7 Ms sample, but much of our analysis focuses on the central (off-axis angles $< 5'.7$) region, which contains a large, faint ALMA sample of $75 > 4.5\sigma$ 850 μm sources. We measure the 850 μm fluxes at the X-ray positions using the ALMA images, where available, or an ultradeep SCUBA-2 map. We find that the full X-ray sample produces $\sim 10\%$ of the 850 μm extragalactic background light. We separate the submillimeter detected X-ray sources into star-forming galaxies and AGNs using a star formation rate (SFR) versus X-ray luminosity calibration for high SFR galaxies. We confirm this separation using the X-ray photon indices. We measure the X-ray fluxes at the accurate positions of the 75 ALMA sources and detect 70% at $> 3\sigma$ in either the 0.5–2 or 2–7 keV bands. However, many of these may produce both their X-ray and submillimeter emission by star formation. Indeed, we find that only 20% of the ALMA sources have intermediate X-ray luminosities (rest-frame 8–28 keV luminosities of $10^{42.5}\text{--}10^{44}$ erg s^{−1}), and none has a high X-ray luminosity ($> 10^{44}$ erg s^{−1}). Conversely, after combining the CDF-S with the CDF-N, we find extreme star formation ($\text{SFR} > 300 \text{ M}_{\odot} \text{ yr}^{-1}$) in some intermediate X-ray luminosity sources but not in any high X-ray luminosity sources. We argue that the quenching of star formation in the most luminous AGNs may be a consequence of the clearing of gas in these sources.

Keywords: cosmology: observations — galaxies: distances and redshifts — galaxies: evolution — galaxies: starburst

1. INTRODUCTION

In the ‘starburst-active galactic nucleus (AGN) connection’ picture, star formation and accretion occur coevally over cosmic time and are together responsible for the growth of galaxies and their resident supermassive black holes. The search for evidence in support of this picture has generated great interest in determining the amount of dusty star formation taking place in sources selected from deep *Chandra* X-ray samples (e.g., Barger et al. 2001, 2015; Lutz et al. 2010; Shao et al. 2010; Harrison et al. 2012; Page et al. 2012; Rosario et al. 2012; Stanley et al. 2015, 2018; Scholtz et al. 2018; Ramasawmy et al. 2019). Unfortunately, this has been a challenging undertaking. Much of what we know about distant, dusty galaxies comes from single-dish submillimeter surveys, whose poor resolution and source con-

fusion make it both difficult to identify counterparts at other wavelengths and to probe the submillimeter flux levels needed to obtain $> 3\sigma$ detections of individual X-ray sources. For example, most of the previous work focused on 250 μm *Herschel* data, where the beam full-width half maximum (FWHM) size is $\sim 18''$, and the one source per 40 beams confusion noise is 19 mJy (Nguyen et al. 2010). Thus, these investigations had to rely on averaging or stacking analyses, in which submillimeter fluxes are either measured at the X-ray (or optical counterpart) positions and then averaged, or are directly measured from stacked submillimeter images of the X-ray (or optical counterpart) sources. All of the X-ray sources in a given X-ray luminosity bin contribute to the mean submillimeter flux for that bin, whether or not they are detected individually.

Barger et al. (2015) were able to go beyond stacking analyses by using ultra-deep SCUBA-2 observations of the *Chandra* Deep Fields (CDFs; the latest SCUBA-2 catalogs can be found in earlier papers in the SUPER GOODS series, i.e., Cowie et al. 2017 and 2018, hereafter, C17 and C18), where the beam FWHM size is $14''$ but the confusion is only 1.65 mJy at $850\,\mu\text{m}$. In combination with the *Spitzer* and *Herschel* data, they performed spectral energy distribution (SED) fits to determine the far-infrared (FIR) luminosities of individual X-ray sources in the 2 Ms CDF-North (CDF-N; Alexander et al. 2003) and the then-4 Ms CDF-South (CDF-S; Xue et al. 2011; Lehmer et al. 2012). They found that the mean values of the FIR luminosity distributions were dominated by a small number of high-luminosity galaxies. This led them to conclude that averaging or stacking analyses overestimate the level of star formation taking place in the bulk of the X-ray sample and hence should be used with caution. They also found that most of the host galaxies of the $L_{2-8\text{ keV}} > 10^{44}\text{ erg s}^{-1}$ AGNs at $z > 1$ were not strong star formers, perhaps because their star formation was suppressed by AGN feedback.

Some recent analyses have looked at the distribution functions of star formation rates (SFRs) and specific SFRs (sSFRs) for X-ray AGNs using high-resolution ALMA images to refine the SFRs (e.g., Stanley et al. 2018; Scholtz et al. 2018). Scholtz et al. (2018) argued, consistent with many previous analyses by this group and others, that any difference between intermediate and high X-ray luminosity samples (i.e., $10^{43} < L_{2-10\text{ keV}} < 10^{44}\text{ erg s}^{-1}$ versus $L_{2-10\text{ keV}} > 10^{44}\text{ erg s}^{-1}$) at $1.5 < z < 3.2$ are subtle. However, these analyses are based on a rather small number of $850\,\mu\text{m}$ detections (e.g., Scholtz et al. 2018 have only 8 $> 4\sigma$ detections in the deep central regions of the CDF-S, as compared to 52 in the present work split as 36 ALMA and 16 SCUBA-2) and on the shallower 4 Ms *Chandra* data rather than the current 7 Ms image (Luo et al. 2017; hereafter, L17).

In the present work, we measure the $850\,\mu\text{m}$ fluxes of the X-ray sources in the L17 catalog using ALMA (this includes all of the brighter submillimeter sources) and SCUBA-2. Conversely, we measure the X-ray properties of the ALMA sources using the *Chandra* images. We also provide optical/NIR spectral classifications for the L17 sources where we have spectra.

We analyze the submillimeter distribution versus X-ray luminosity to determine how the submillimeter sources relate to the X-ray sources. We will argue that clear and significant differences emerge between the intermediate and high X-ray luminosity populations: the intermediate X-ray luminosity sources have a submillimeter distribution that is much more skewed to high submillimeter fluxes. We discuss how this might suggest gas clearing.

2. DATA AND METHODS

2.1. X-ray Data

We began with the X-ray catalog of L17 based on the 7 Ms observations of the CDF-S. This catalog contains 1008 significant sources, but we restrict our analysis to off-axis angles $< 10'$ (hereafter referred to as *the full region*) where, as we discuss below, a deep SCUBA-2 $850\,\mu\text{m}$ map exists with rms noise less than $< 1.5\text{ mJy}$. This reduces the sample to 938 X-ray sources. We hereafter refer to this as *the full X-ray sample*. We plot observed 0.5–2 keV flux versus off-axis angle for the full X-ray sample in Figure 1.

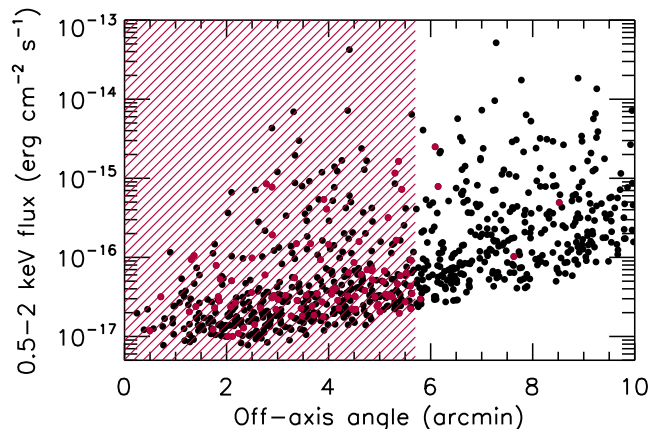


Figure 1. Observed 0.5–2 keV flux vs. *Chandra* off-axis angle for the X-ray sources lying within the SCUBA-2 map region where the $850\,\mu\text{m}$ noise is less than 1.5 mJy (black circles). The deepest SCUBA-2 observed area of 100 arcmin^2 (red shading) was also the most intensively targeted with ALMA (non-contiguous combined ALMA area of 5.9 arcmin^2 ; see Section 2.2). The red circles show X-ray sources that lie in the ALMA images (note that some of these lie outside the red shaded region).

In the soft (0.5–2 keV) band, the sensitivity (from L17) rises from a value of $7 \times 10^{-18}\text{ erg cm}^{-2}\text{ s}^{-1}$ on-axis, to $2 \times 10^{-17}\text{ erg cm}^{-2}\text{ s}^{-1}$ at $5.7'$ (the edge of the region with intensive ALMA observations, hereafter referred to as *the central region*; see Section 2.2), to just over $10^{-16}\text{ erg cm}^{-2}\text{ s}^{-1}$ at the $10'$ outer radius. In the hard (2–7 keV) band, the sensitivities are about a factor of 5 higher.

526 sources from the full X-ray sample lie in the central region. We hereafter refer to these as *the central region X-ray sample*. We list the full X-ray sample in Table 1, ordered by *Chandra* off-axis angle so that the most central sources appear first.

2.2. Submillimeter Data

The CDF-S has deep $850\,\mu\text{m}$ observations made with the SCUBA-2 camera on the JCMT, together with a

large number of targeted ALMA band 7 observations. (We refer to all the submillimeter fluxes as $850\ \mu\text{m}$, ignoring the small differences in the ALMA band 7 wavelength centers for different programs.) The SCUBA-2 observations are very deep in the $100\ \text{arcmin}^2$ central region (red shading in Figure 1) with rms noise $< 0.5\ \text{mJy}$ throughout nearly all of the central region. Beyond the central region, they degrade with off-axis angle, reaching rms noise of $1.4\ \text{mJy}$ at the $10'$ outer radius (see Figure 3). In the central region, all of the $> 2.25\ \text{mJy}$ $850\ \mu\text{m}$ SCUBA-2 sources have been observed with ALMA in band 7, together with a number of fainter SCUBA-2 sources. Details of these observations and their reductions may be found in C18. Note that some of the ALMA images are archival observations from Hodge et al. (2013; 4 sources), Mullaney et al. (2015; 8 sources), P.I. G. Barro (1 source), and Schreiber et al. (2017; 1 source). However, we do not incorporate the four additional sources from the ALESS main table of Hodge et al. (2013) that correspond to X-ray sources, as they only have poor-quality cycle0 images; they lie well outside the central region.

We restrict the area of the individual ALMA images to their FWHM radius of $8''.75$. With this restriction, the ALMA images cover a (non-contiguous) total area of $7.2\ \text{arcmin}^2$, with most of that area (that is, $5.9\ \text{arcmin}^2$) concentrated in the central region. In Figure 1, we show $0.5\text{--}2\ \text{keV}$ flux vs. off-axis angle for the X-ray sources lying within the SCUBA-2 region with rms noise is $< 1.5\ \text{mJy}$ (black circles). We use red circles to denote those sources that are also covered by the ALMA images.

As an aside, we note that 17 of the 20 $1.1\ \text{mm}$ detected sources from the $69\ \text{arcmin}^2$ GOODS-S ALMA survey of Franco et al. (2018) comprise a subset of the C18 sample (with the three remaining sources considered false detections by Franco et al.). Moreover, eight of the 12 $1.2\ \text{mm}$ detected sources from the $20\ \text{arcmin}^2$ ASAGAO ALMA survey (Ueda et al. 2018) are also contained in the C18 sample. Two of their remaining four sources are not detected at the 4.5σ level (S/N of 4.3 and 4.2) and have no counterparts at other wavelengths. These sources are also not detected at the 2σ level in SCUBA-2 and are probably false. Their other two sources (S/N of 5.2 and 4.4) both have counterparts at other wavelengths.

Thus, the SCUBA-2 selected C18 ALMA sample recovers all reliable $1.1\text{--}1.2\ \text{mm}$ sources from the shallow mosaicked ALMA surveys of the CDF-S for a much smaller investment of ALMA time. Even for the deeper $4.5\ \text{arcmin}^2$ Hubble Ultra Deep Field ALMA survey of Dunlop et al. (2017), we detected all three of their sources with $1.3\ \text{mm}$ fluxes $> 800\ \mu\text{Jy}$ but not their two fainter sources with fluxes around $300\ \mu\text{Jy}$ ($> 5\sigma$).

2.3. X-ray Fluxes of the ALMA Sources

C18 gives a catalog of 75 ALMA $850\ \mu\text{m}$ sources with extremely accurate positions (their Table 4). The $850\ \mu\text{m}$ fluxes extend to less than $1\ \text{mJy}$. Comparing

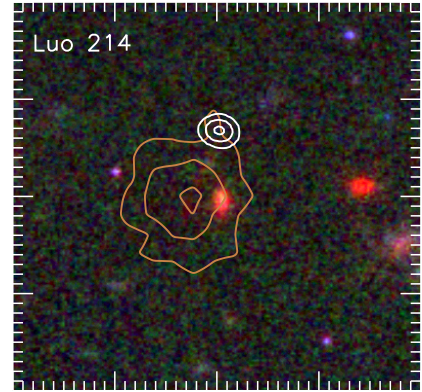


Figure 2. Contour plot of L17 #214 using the *Chandra* $0.5\text{--}2\ \text{keV}$ 7 Ms observations (orange contours). The white contours show the ALMA $850\ \mu\text{m}$ image of C18 #2. Both sets of contours are plotted at 0.2, 0.5, and 0.9 times the respective maximum values. The contours are overlaid on the F435W (blue), F850LP (green), and F160W (red) images from the *HST* ACS and CANDELS data. The image is $10''$ on a side.

the ALMA coordinates with the L17 coordinates gives an absolute astrometric offset of $0''.0$ in R.A. and $0''.2$ in decl. We applied this small astrometric correction to the ALMA positions.

If an ALMA source has a counterpart in the L17 catalog within $1''$, then we take the X-ray flux from the catalog. The matching is relatively insensitive to the choice of matching radius, which is based on the 2σ positional uncertainties in the fainter *Chandra* sources from L17. This provides X-ray fluxes for 41 of the 75 ALMA sources. The mean of the offsets between the ALMA and L17 positions for these sources is $0''.46$.

For the remaining 34 ALMA sources, we measured the $0.5\text{--}2\ \text{keV}$ or $2\text{--}7\ \text{keV}$ fluxes in the L17 images using the procedure outlined in Cowie et al. (2012) and briefly described below. One ALMA source (C18 #2) is close enough to an X-ray source (i.e., L17 #214) for the X-ray flux measured at the ALMA position to be contaminated by the X-ray emission from the neighbor (Figure 2), so we do not use its X-ray flux.

We used a circular aperture to calculate the X-ray fluxes, which provides a good approximation to the point spread function (PSF) shape at these small off-axis angles. We adopted a $1''.25$ aperture radius, which offers a good compromise between including most of the counts, maximizing the signal-to-noise (S/N), and minimizing the contamination from neighboring sources. With the aperture specified, we computed the X-ray counts s^{-1} as $C = (S - B)/t$, where S is the number of counts in the aperture, $B (= \pi r^2 b)$ is the number of background counts expected in the same aperture, and t is the effective

tive exposure time at the position of this aperture. We measured the mean background b (counts arcsec $^{-2}$) in an $8''$ – $22''$ annulus around the source after clipping pixels with more than 4 counts. (An extensive discussion of this choice may be found in Cowie et al. 2012.) C may be negative or positive. We converted the counts to fluxes using a single normalization, which we chose by comparing the aperture fluxes that we measured for sources in the L17 catalog with the L17 fluxes. We found good agreement with a scatter of 23%, which is adequate for the present work.

If an ALMA source is detected at $> 3\sigma$ in either the 0.5–2 keV or 2–7 keV band, then we considered the source to be X-ray detected. With this procedure, nine more ALMA sources are X-ray detected (for a total of 50). In Table 2, we summarize the X-ray properties of the 75 ALMA sources (giving no X-ray fluxes for C18 #2). In the 0.5–2 keV band, there are a total of 47 ALMA sources detected. In the 2–7 keV band, there are a total of 26 ALMA sources detected, all but 3 of which are also detected in the 0.5–2 keV band.

2.4. Submillimeter Fluxes of the X-ray Sources

Where the X-ray sources have an ALMA counterpart within the 2σ positional uncertainties quoted by L17, we used the best submillimeter fluxes and rms noise of C18 (Columns 8 and 9 of their Table 4). 41 X-ray sources have direct ALMA detections ($> 4.5\sigma$) in the ALMA images.

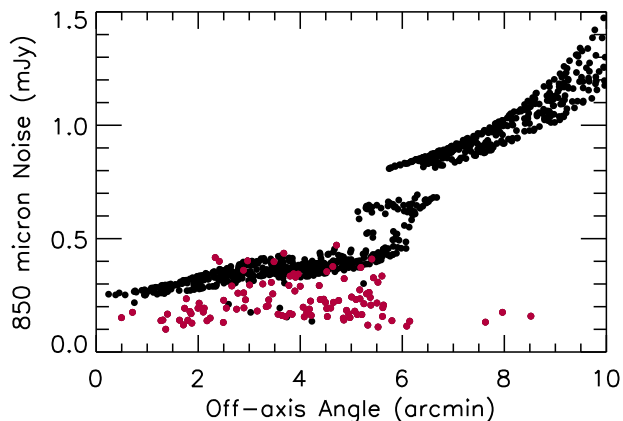


Figure 3. Locally determined 850 μ m rms noise measurements for the sources in the full X-ray sample vs. off-axis angle (black circles—SCUBA-2 measurements, since these X-ray sources do not lie in the ALMA observed areas; red circles—ALMA measurements). The jump at 6' reflects the degrading sensitivity in the off-axis SCUBA-2 images. It corresponds to the position interior to which the SCUBA-2 maps are dominated by the more compact (DAISY) scan patterns. (See C18 for an extensive discussion.)

For the X-ray sources that lie within the ALMA images but do not have direct ALMA detections (i.e., there is no corresponding $> 4.5\sigma$ submillimeter source), we measured the highest peak submillimeter flux within $1''$ of the X-ray source, along with the corresponding locally determined rms noise. This choice of radius is large relative to the measured dispersion between the X-ray and ALMA positions (see Section 2.3). In order to correct for the upward biasing introduced by the peaking up procedure, we applied a -0.41 mJy correction to each flux based on measurements made at random positions. We show the ALMA rms noise measurements as red circles in Figure 3. We stress that we made all of the above measurements on primary beam corrected images. We also did not make any measurements outside the ALMA FWHM radius (see Section 2.2).

We next subtracted from the SCUBA-2 image all of the direct ALMA detections ($> 4.5\sigma$) in the ALMA images, smoothed to the SCUBA-2 PSF (see Figure 8 of C18). This minimizes contamination from the wings of the bright submillimeter sources. We then measured the SCUBA-2 fluxes and rms noise from the cleaned SCUBA-2 image for all of the remaining X-ray sources. We show the SCUBA-2 rms noise measurements as black circles in Figure 3.

109 of the X-ray sources lie in the ALMA images with typical rms noise ~ 0.1 – 0.3 mJy. These sources are shown with red circles in Figure 3. The rms noise of the remaining X-ray sources measured from the SCUBA-2 cleaned image are higher, ~ 0.3 – 0.5 mJy in the central region (see Figure 3). We note that the latter does not include confusion noise, which may be comparable to the systematic noise in this region (see C17).

If an X-ray source is detected at $> 3\sigma$ at 850 μ m, then we consider the source to be submillimeter detected. In the central region, 27 X-ray sources have submillimeter detections above 2.25 mJy and 37 above 1.65 mJy ($\sim 7\%$ of the central region X-ray sample). All of the sources with submillimeter fluxes above 2.25 mJy are ALMA fluxes, while 4 of the 37 above 1.65 mJy are SCUBA-2 fluxes. Tests on randomized positions show that, on average, one of the detections above 1.65 mJy and none above 2.25 mJy will be false positives.

2.5. Spectroscopic Redshifts and Spectral Classifications

L17 determined the most probable optical/NIR counterparts to the X-ray sources based on both the 2σ positional uncertainties of the X-ray sources and the magnitudes of the potential counterparts. We adopt the Taiwan ECDF-S Near-Infrared Survey (TENIS) K_s magnitudes (Hsieh et al. 2012) provided in the L17 catalog. We show these magnitudes versus 0.5–2 keV flux for the full X-ray sample in Figure 4(a).

L17 next compiled redshifts from the literature for their most probable counterparts. From our full X-ray sample of 938 sources, L17 found 529 (56%) had red-

shifts considered secure by whichever group made the measurement. For a small number of these, the X-ray source lies within the envelope of a bright galaxy, but it is significantly separated from the galaxy’s center. In these cases, we assumed that the X-ray source was associated with the galaxy, and we assigned the redshift to the X-ray source. However, it is possible that the X-ray source is projected (i.e., an unrelated background source).

We compiled all of the publicly available spectra for these counterparts (see Popesso et al. 2009; Balestra et al. 2010; Cowie et al. 2012 and references therein; see also the notes given in Table 1), together with 377 spectra that we observed ourselves using the DEIMOS (Faber et al. 2003) (357 sources), LRIS (Oke et al. 1995) (13 sources) and MOSFIRE (McLean et al. 2012) (7 sources) spectrographs on the Keck 10 m telescopes. Details of how we reduced the spectra can be found in Cowie et al. (1996; 2016).

We visually inspected the spectra for each counterpart and decided whether the redshift identification was robust. We also assigned a rough spectral class—broad-line AGN (BLAGN), Seyfert type 2 (Sy2), absorber (Abs), and star-forming galaxy (SFG)—to each spectrum. We classified as BLAGNs the sources that have some lines in their spectra with $\text{FWHM} > 2000 \text{ km s}^{-1}$. Note that one object (L17 #185) is a broad absorption line quasar, or BALQSO. We classified as Sy2s the sources where high excitation narrow lines are present (usually CIV $\lambda 1549$, CIII $\lambda 1909$, or [NeV] $\lambda 3426$; see, e.g., Szokoly et al. 2004). We classified as SFGs the sources with UV absorption lines or $\text{EW}([\text{OII}]) > 10 \text{ \AA}$ and no broad or high-ionization lines, and as Abs the sources with no strong emission lines but strong absorption features. The spectral classifications are subject to the lines that are visible in the available wavelength coverage and so may have some redshift dependence.

In this way, we assigned secure redshifts and spectral classifications to 64% of the sources in our full X-ray sample (596 sources out of 938, including 10 stars).

We could not spectrally classify 17 of the sources in our full X-ray sample that were cataloged in L17 as having secure redshifts. Based on the totality of the spectral data available, we concluded that 10 of these do not have a secure redshift. For the remaining seven, either the spectra were not available to us, or they were insufficient for us to make a spectral classification, but we still adopted the redshift. We also added a further two secure redshifts from the MOSDEF sample of Kriek et al. (2015) for which we could not make spectral classifications. Thus, in total, 605 sources in our full X-ray sample have secure redshifts (64.5%), 596 of which also have spectral classifications. We illustrate this in Figure 4(a), where we plot K_s magnitude versus $0.5\text{--}2 \text{ keV}$ flux. We use red squares (or green circles for stars) to denote X-ray sources with both a secure redshift and

a spectral classification, and we use blue diamonds to denote unclassified sources.

In contrast, in Figure 4(b), we show how for the submillimeter detected X-ray sources, we only have secure redshifts for 50% (53 out of the 105 sources with $850 \mu\text{m}$ fluxes $> 3\sigma$, of which 51 also have spectral classifications). This presumably reflects that these sources are dustier, higher redshift, and have fainter K_s magnitudes, which makes them more difficult to identify with optical/NIR spectra.

We summarize the secure spectroscopic redshifts (hereafter, *speczs*) and spectral classifications for the full X-ray sample in Table 1, where we also give the submillimeter fluxes and rms noise (see Section 2.4). In the full X-ray sample, there are 22 BLAGNs, none of which is detected at $> 3\sigma$ at $850 \mu\text{m}$ (the one BALQSO is also not detected); 47 Sy2s, 8 of which are detected; 388 SFGs, 38 of which are detected; and 128 Abs, 5 of which are detected. The largest number of submillimeter detected sources occurs in the category without spectral classifications (no IDs; 54 out of 342), as might be expected given the higher obscuration and higher redshifts of submillimeter sources in general.

2.6. Photometric Redshifts

There has been a large number of papers estimating photometric redshifts (hereafter, *photzs*) in the CDFS (e.g., Santini et al. 2009, 2015; Rafferty et al. 2011; Dahlen et al. 2013; Hsu et al. 2014; Skelton et al. 2014; Straatman et al. 2016). Rather than recompute *photzs* ourselves, we use the literature estimates here. However, we caution that in C18, we found considerable scatter in the estimates from the different literature catalogs for the optical/NIR faint submillimeter sources.

We compared the *photzs* from the literature catalogs that use the deep *Spitzer* IRAC data of either Ashby et al. (2013) or Labbé et al. (2015) and are purely photometrically based (i.e., Hsu et al. 2014, hereafter, H14; Santini et al. 2015; Straatman et al. 2016, hereafter, S16) against the *speczs* in Table 1. We found that they each have a significant number of outliers, which we define as $(\text{photz-specz})/\text{specz} > 0.1$. (Note that our outlier definition is tighter than that of L17, who used > 0.15 .) All three catalogs have 9–10% of outliers, but H14 has a much lower percentage of outliers than the other two catalogs when considering only the X-ray sources with AGN spectral signatures. Thus, we adopt the *photzs* first from H14, and if they do not have one, then from S16 (after restricting to sources with their quality flag $Q < 3$). All but 44 of the X-ray sources have either *speczs* or *photzs*, and of those 44, all but one are faint ($K_s > 25$). The brighter source is closely blended with a brighter galaxy.

In Column 12 of Tables 1 and 2, we give the adopted *photzs* for the full X-ray sample and the ALMA sample, respectively. Additionally, in Table 2 we provide a FIR-based redshift estimate from C18 in brackets if there is

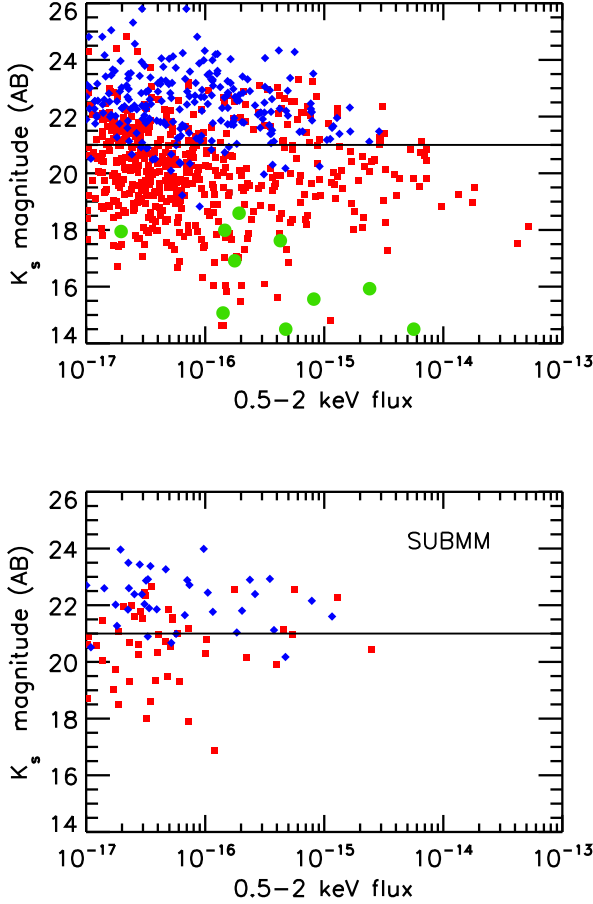


Figure 4. K_s magnitude vs. observed 0.5–2 keV flux for (a) the full X-ray sample and (b) those sources in the full X-ray sample that are detected at $> 3\sigma$ at $850\ \mu\text{m}$. Red squares denote X-ray sources with both a secure redshift and a spectral classification (in (a), this includes 10 stars, denoted by green circles), while the remaining sources are denoted by blue diamonds. Brighter than $K_s = 21$ (horizontal line), most of the sources have both a secure redshift and a spectral classification: (a) 415 sources out of 442, or 94%, and (b) 29 sources out of 34, or 85%.

no specz or high-quality photz available. In Figure 5, we compare the photzs and speczs for sources in the full X-ray sample with both a specz and a photz (black circles). We mark the outliers by enclosing them in open squares. The photzs for the BLAGNs and the Sy2s (blue and green, respectively) are generally well estimated.

There are only a handful of X-ray sources with high redshifts (nine sources above $z = 4$ and two above $z = 5$), almost all of which are based on photzs (see Cowie et al. 2019 for a detailed discussion of these very high-redshift AGN candidates). Most of the X-ray sources lie at low redshifts, with 570 (58%) below

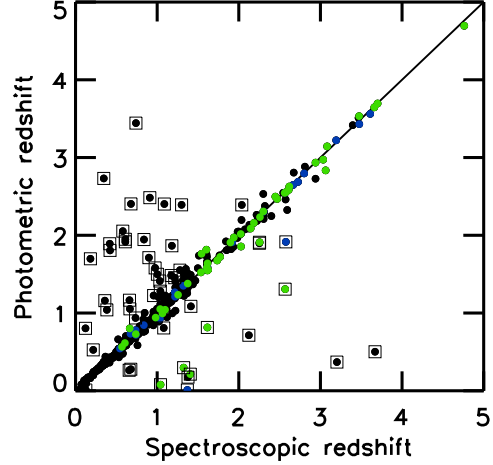


Figure 5. Adopted photzs from H14 and S16 vs. secure speczs for sources in the full X-ray sample with both a specz and a photz (black circles). The BLAGNs are shown in blue, and the Sy2s in green. Outliers are enclosed in open squares.

$z = 1.6$. Most of these low-redshift sources have spectroscopic identifications (501 sources).

2.7. X-ray Luminosities

Given the high redshifts of the submillimeter detected sources (see Figure 25 of C18), we calculate the rest-frame X-ray luminosities from

$$L_{2-8\ \text{keV}}^R = 4\pi d_L^2 f_{0.5-2\ \text{keV}} ((1+z)/4)^{\Gamma-2} \text{ erg s}^{-1}, \quad (1)$$

and

$$L_{8-28\ \text{keV}}^R = 4\pi d_L^2 f_{2-7\ \text{keV}} ((1+z)/4)^{\Gamma-2} \text{ erg s}^{-1}, \quad (2)$$

where d_L is the luminosity distance, and we take the photon index $\Gamma = 1.8$. These equations are exact for sources at $z = 3$, but the K-correction term may be less appropriate for lower redshift sources. We have not corrected the luminosities for X-ray absorption, which could potentially have a non-negligible effect, particularly for the lower energy band. We will consider absorption corrected luminosities in the Discussion.

3. $850\ \mu\text{m}$ PROPERTIES OF THE X-RAY SAMPLE

The $850\ \mu\text{m}$ flux is a rough measure of the FIR luminosity and hence of the SFR, independent of redshift (Blain & Longair 1993). In rough terms, a 2 mJy source corresponds to a $\text{SFR} \approx 300\ M_\odot \text{ yr}^{-1}$ for a Kroupa (2001) initial mass function (IMF); see Equation 5 of C17, which gives

$$\text{SFR} (M_\odot \text{ yr}^{-1}) = (143 \pm 20) \times S_{850\ \mu\text{m}} (\text{mJy}). \quad (3)$$

This SFR is not usually affected by AGN contributions, since the torus is generally too hot to contribute to the $850\ \mu\text{m}$ flux, even at high redshifts (e.g., Hatziminaoglou et al. 2010).

3.1. 850 μm Signal

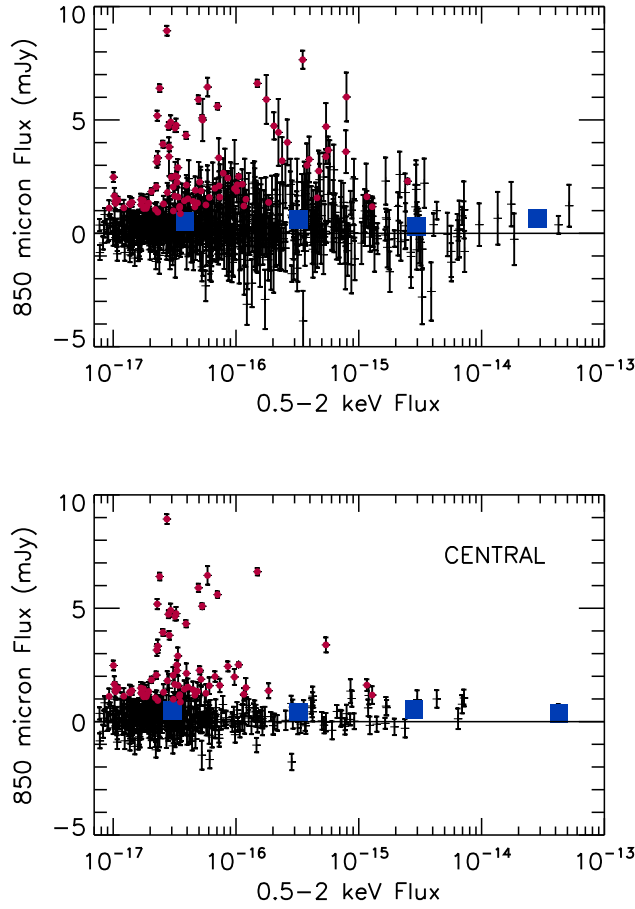


Figure 6. Measured 850 μm flux vs. 0.5–2 keV flux (black with 1σ uncertainties) for the (a) full and (b) central region X-ray samples. The red circles show the sources with $> 3\sigma$ 850 μm detections. The blue squares show the mean 850 μm flux per X-ray source (here the uncertainties are generally smaller than the symbol size).

In Figure 6(a), we show measured 850 μm flux versus 0.5–2 keV flux for the full X-ray sample. The X-ray sources contain a significant 850 μm flux with a mean of 0.52 mJy per X-ray source, or just over a SFR of $70 M_{\odot} \text{ yr}^{-1}$. The 95% confidence range is 0.44 to 0.61 mJy. As can be seen from the blue squares, this contribution is similar at all X-ray fluxes. We also find a similar value for the central region X-ray sample (Figure 6(b)), where both the X-ray and submillimeter data are much more sensitive. Here the mean 850 μm flux is 0.49 mJy per X-ray source, with a 95% confidence range of 0.39–0.60 mJy. However, a Kolmogorov-Smirnov test gives a less than 1% probability that either of the distributions is normal, and the medians are substantially

lower: 0.26 mJy for the full sample, and 0.22 mJy for the central sample.

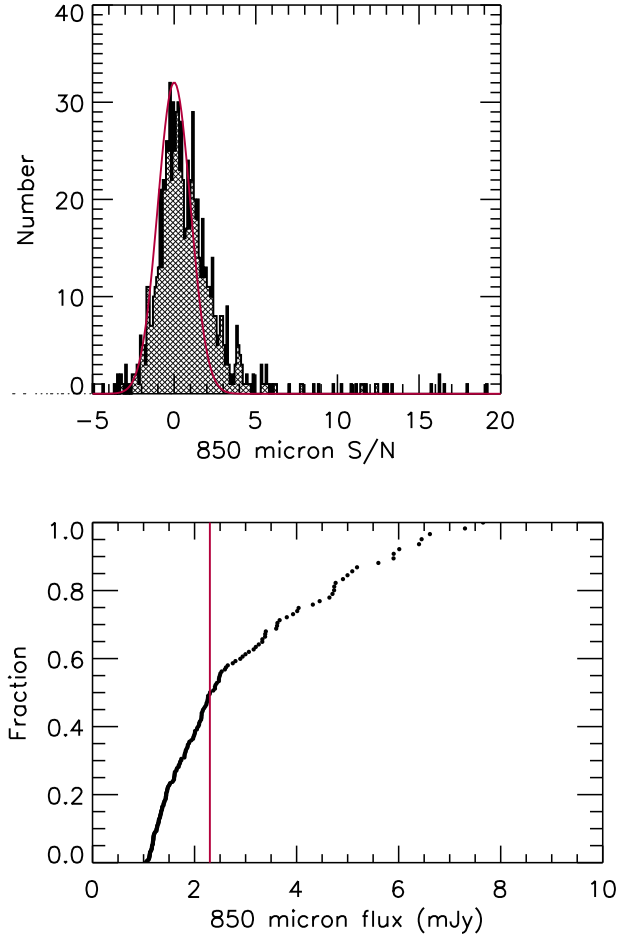


Figure 7. (a) S/N distribution for the 850 μm measurements of the full X-ray sample (gray shading). The red curve shows the expected distribution in the absence of any submillimeter signal in the X-ray sample. (b) Cumulative contribution with increasing 850 μm flux to the total measured 850 μm light from the full X-ray sample. 50% of the light comes from the 57 (out of 938) sources with fluxes above 2.3 mJy (red vertical line).

Nearly all of the 850 μm signal comes from the sources that are significantly detected. Barger et al. (2015) found a similar result for the GOODS-N. In Figure 7(a), we show the S/N distribution (gray shading), which illustrates the skewness and kurtosis of the measurements. The bulk of the X-ray sources are consistent with having no 850 μm flux. The red curve shows the expected distribution in this case. The sources producing most of the 850 μm flux lie in the very extended tail. This illustrates the dangers of using simple stacking analyses on this type of data, where a very small number of sources dominate the mean and are poorly representa-

tive of the great majority of the sample. To emphasize this point, in Figure 7(b), we show the cumulative contribution to the total measured 850 μm light from the full X-ray sample. 50% of the light comes from the 57 (out of 938) sources with fluxes above 2.3 mJy.

3.2. Contributions to the 850 μm Extragalactic Background Light

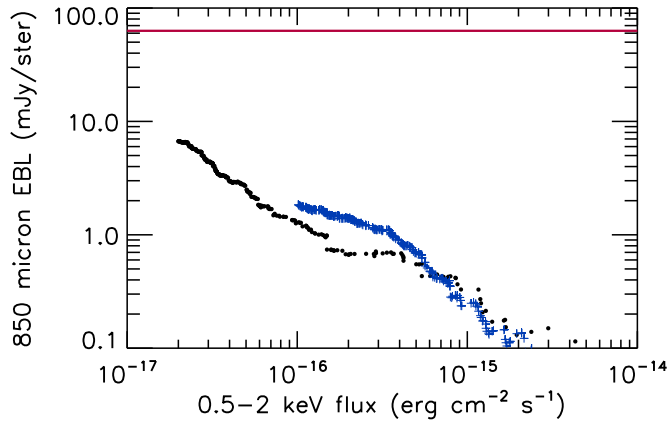


Figure 8. 850 μm EBL produced by the full (blue crosses; down to the 0.5–2 keV completeness level of 10^{-16} $\text{erg cm}^{-2} \text{s}^{-1}$) and central region (black circles; down to the deeper 0.5–2 keV completeness level of 2×10^{-17} $\text{erg cm}^{-2} \text{s}^{-1}$) X-ray samples vs. 0.5–2 keV flux. The red horizontal line shows the 850 μm EBL from Fixsen et al. (1998). Because there are more bright X-ray sources in the full X-ray sample, it is a better estimator of the contributions to the EBL from the brighter X-ray fluxes, while the deeper central X-ray sample is a better estimator of the contributions from the fainter X-ray fluxes.

In Figure 8, we show the contributions above a given 0.5–2 keV flux to the 850 μm extragalactic background light (EBL) from the full X-ray sample down to its completeness level of 10^{-16} $\text{erg cm}^{-2} \text{s}^{-1}$ (blue crosses) and from the central region X-ray sample down to its deeper completeness level of 2×10^{-17} $\text{erg cm}^{-2} \text{s}^{-1}$ (black circles). The contributions rise rapidly with decreasing X-ray flux. At the limits of the *Chandra* 7 Ms data, $\sim 10\%$ of the 850 μm EBL measured by Fixsen et al. (1998) is identified by the X-ray sources (which encompasses more than just AGNs, see below). Deep blank-field SCUBA-2 surveys recover $\sim 30\%$ of the Fixsen et al. 850 μm EBL measurement (e.g., Zavala et al. 2017), which means most of that submm light is not being identified by the X-ray sources, even though the sensitivity of the central region of the CDF-S data is such that we could detect Compton-thin X-ray AGNs out to beyond $z \sim 6$ (see Figure 1 of Cowie et al. 2019). As we discuss

below, some of the X-ray light in the submillimeter detected X-ray sources is due to star formation rather than AGN activity, so this constraint is even more severe.

3.3. Star-Forming Galaxies versus AGNs

We preface this section by emphasizing that we have not corrected our X-ray luminosities for absorption (see Section 2.7), which could cause some uncertainties in the luminosity bins that we adopt. However, by focusing on a 2–7 keV selected sample, we will be less sensitive to obscuration effects for Compton-thin AGNs than we would be with a 0.5–2 keV selected sample, though we need to keep in mind that even a 2–7 keV selected sample will not be able to probe very Compton-thick AGNs.

In Figure 9, we show 850 μm flux versus (a) $L_{2-8 \text{ keV}}^R$ and (b) $L_{8-28 \text{ keV}}^R$ for the central region X-ray sample. We only show sources with $z > 1$ (specz and photz), since for these redshifts, the 850 μm flux is a good measure of the FIR luminosity. Sources that are only detected in one X-ray band and hence are only present in one panel are shown with black circles (or, in the case of the two Sy2s in Figure 9(b), black circles with green interiors). We obtained the star formation locus (red curve in each panel), where both the X-ray luminosity and the 850 μm flux are consistent with being produced by star formation, using Mineo et al. (2012)’s L_X -SFR relation (from their Section 8.1, but for a Kroupa 2001 IMF and our X-ray luminosities) and C17’s SFR- $f_{850 \mu\text{m}}$ relation (their Equation 5, which we reproduce as Equation 3 in this paper).

The brightest 850 μm detected X-ray sources, most of which are only detected in the more sensitive 0.5–2 keV band (i.e., black circles in Figure 9(a)), are drawn primarily from low X-ray luminosity galaxies. Considering both panels and taking into account expected scatter about the star formation locus, we conclude that all but one of the sources with high 850 μm fluxes (> 4 mJy) are consistent with having both their X-ray luminosity and their 850 μm flux produced by star formation. The exception is L17 #666: this Sy2 has an 850 μm flux of 5.1 ± 0.13 mJy and an $L_{8-28 \text{ keV}}^R = 1.8 \times 10^{43}$ erg s^{-1} , and because it is faint in the 0.5–2 keV band but bright in the 2–8 keV band, it is likely a highly obscured AGN.

There are only eight sources that are strong submillimeter sources (850 μm fluxes > 2.25 mJy, which is roughly the SCUBA-2 $> 4\sigma$ limit through the whole central region) and have X-ray luminosities that clearly classify them as AGNs (here, $L_{8-28 \text{ keV}}^R > 10^{42.5}$ erg s^{-1}). However, these sources are all at intermediate (Seyfert) X-ray luminosities ($L_{8-28 \text{ keV}}^R = 10^{42.5} - 10^{44}$ erg s^{-1}) with a range from $L_{8-28 \text{ keV}}^R = 0.8 - 7.2 \times 10^{43}$ erg s^{-1} ; none of the 19 sources at high (quasar) X-ray luminosities ($L_{8-28 \text{ keV}}^R > 10^{44}$ erg s^{-1}) has an 850 μm flux above 1.6 mJy. Indeed, the mean 850 μm flux for these 19 host galaxies is only 0.46 mJy, which corresponds to a SFR of $\sim 65 M_\odot \text{yr}^{-1}$. We conclude

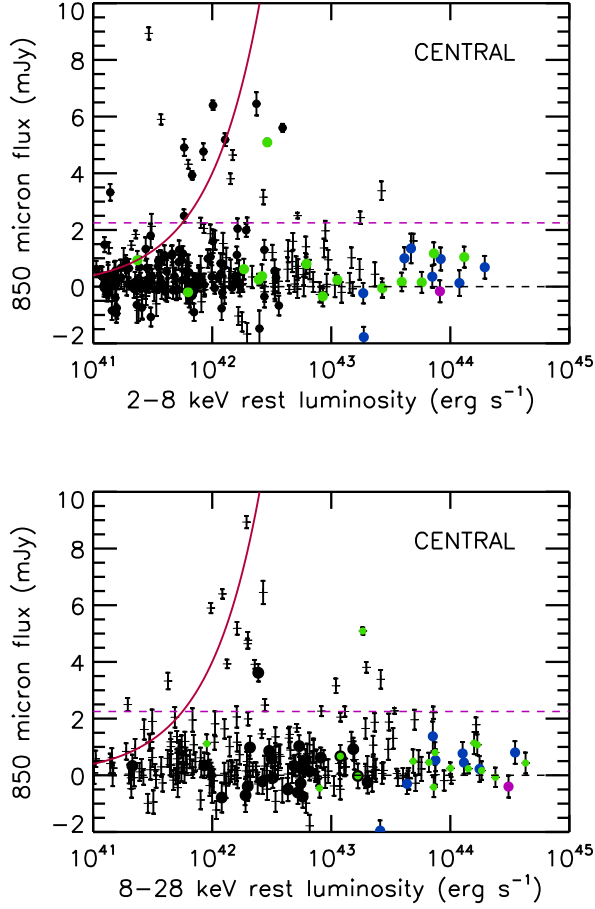


Figure 9. 850 μm flux vs. (a) $L_{2-8 \text{ keV}}^R$ and (b) $L_{8-28 \text{ keV}}^R$ for the central region X-ray sample with $z > 1$ (specz and photz). Blue circles show BLAGNs, green Sy2s, and purple the one BALQSO. All other sources are shown as black plus signs. The uncertainties are $\pm 1\sigma$. The red curve shows the relation for sources where the X-rays are due to star formation. Sources not detected in the other X-ray band are shown with black circles. In (a) there are no Sy2s or BLAGNs that satisfy this, while in (b) only two Sy2s do, and they are shown as black circles with green interiors. The purple dashed horizontal line in each panel shows the 2.25 mJy 850 μm limit, which roughly corresponds to the SCUBA-2 $> 4\sigma$ limit through the whole central region.

that extreme SFRs $\gtrsim 300 M_{\odot} \text{ yr}^{-1}$ are only seen at intermediate X-ray luminosities.

In Figure 9(b), we can see that the decline in 850 μm fluxes of individual sources above $\sim 5 \times 10^{43} \text{ erg s}^{-1}$ corresponds roughly to the X-ray luminosity where the BLAGNs and many of the Sy2s begin to appear. We illustrate this more clearly in Figure 10, where we plot 850 μm flux versus spectral class for three bins in X-ray luminosity. The most X-ray luminous (quasar) bin

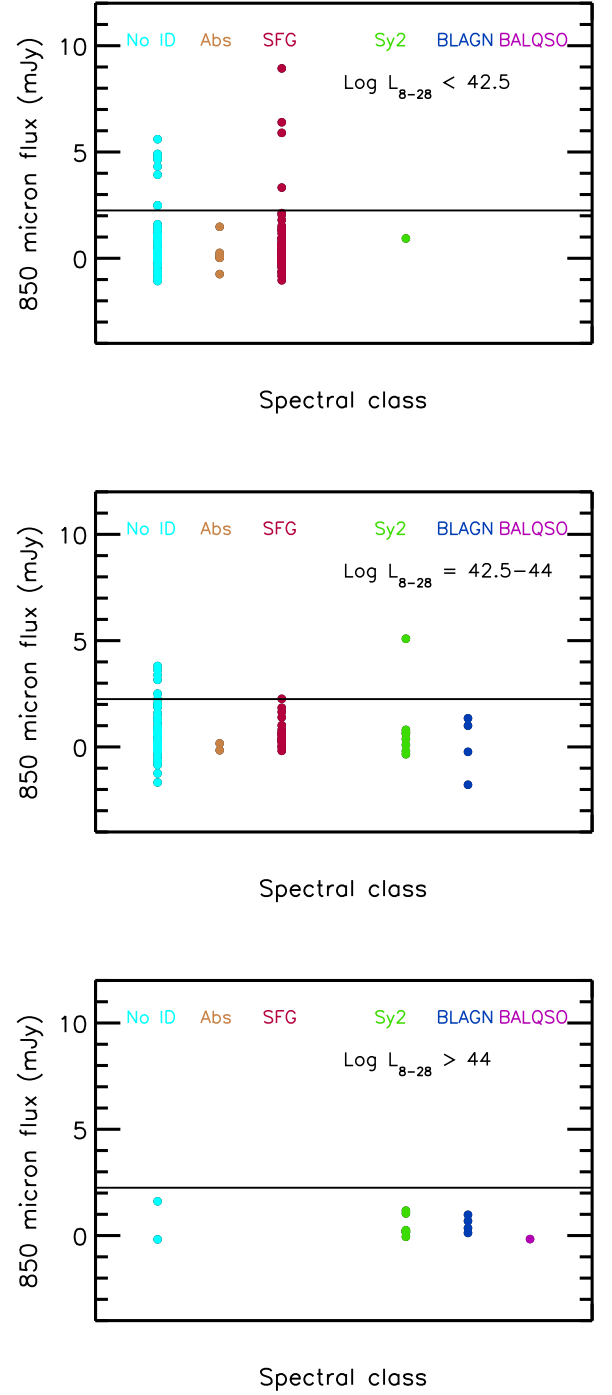


Figure 10. 850 μm flux vs. optical spectral class for the central region X-ray sample with $z > 1$ (specz and photz) and (a) $\log L_{8-28 \text{ keV}}^R < 42.5$, (b) $\log L_{8-28 \text{ keV}}^R = 42.5-44$, and (c) $\log L_{8-28 \text{ keV}}^R > 44$. The optical spectral classifications are color-coded (purple—BALQSO; blue—BLAGNs; green—Sy2s; red—SFGs; gold—Abs; cyan—no IDs). The horizontal line shows the 2.25 mJy 850 μm limit, which roughly corresponds to the SCUBA-2 $> 4\sigma$ limit through the whole central region.

is dominated by BLAGNs and Sy2s, and none of the sources has an $850\ \mu\text{m}$ flux > 2.25 mJy. In the intermediate X-ray luminosity bin, there is a much wider range of spectral classes, and a fraction of the sources (though none of the BLAGNs) have $850\ \mu\text{m}$ fluxes > 2.25 mJy. In the lowest X-ray luminosity bin, SFGs and no IDs dominate, and a significant fraction of these have $850\ \mu\text{m}$ fluxes > 2.25 mJy. For these sources, the X-ray luminosity is likely produced by star formation.

These results suggest that the strongest star formation occurs in less luminous X-ray AGNs, while extreme star formation is not seen in the most luminous X-ray AGNs. We quantify and interpret this result in the Discussion.

4. X-RAY PROPERTIES OF THE SUBMILLIMETER DETECTED X-RAY SOURCES

We now turn to the X-ray properties of the submillimeter detected X-ray sources, and, in particular, to whether the X-ray spectra are consistent with the classifications we inferred from Figure 9. As in Section 3.3, we focus on the central region, where the X-ray and submillimeter observations are the deepest.

We start by considering the properties of the central region X-ray sample with speczs. In Figure 11(a), we plot effective observed photon index, Γ , from L17 versus specz, color-coding the sources by optical spectral class. We show the sources with $L_{8-28\ \text{keV}}^R > 10^{42.5}\ \text{erg s}^{-1}$ with larger symbols. We enclose in an open square any source with a $> 3\sigma$ submillimeter detection.

Only one of the sources classified as an AGN from the optical/NIR spectra—the Sy2 galaxy L17 #666 discussed in Section 3.3—has a submillimeter detection (green circle enclosed in an open square in Figure 11(a)). Note that the BLAGNs (blue) all have nearly identical photon indices: in the central region, the mean photon index is $\bar{\Gamma} = 1.62$ (blue line in Figure 11(a)), and in the full sample, $\bar{\Gamma} = 1.65$. Their uniformity is consistent with there being very little absorption in their X-ray spectra. In contrast, the Sy2s (green) have a wide range in Γ corresponding to a large spread in the absorption column densities.

The bulk of the X-ray sources with speczs that are submillimeter detected (enclosed in open squares) are classified as SFGs (24) based on their optical/NIR spectra. Most of these have a soft Γ and a low X-ray luminosity, consistent with being star formation dominated (e.g., Sazonov & Khabibullin 2017 give $\Gamma = 2.1 \pm 0.1$ for the collective X-ray spectrum of luminous, high-mass X-ray binaries; black line in Figure 11). All six of the submillimeter detected SFGs with $\Gamma < 0.7$ are at relatively low redshifts ($z < 1.4$). These probably contain an obscured AGN.

Five Abs sources are also detected in the submillimeter, all at low redshifts ($z < 1.1$). Four have soft Γ consistent with being X-ray binary dominated, but one has a hard Γ .

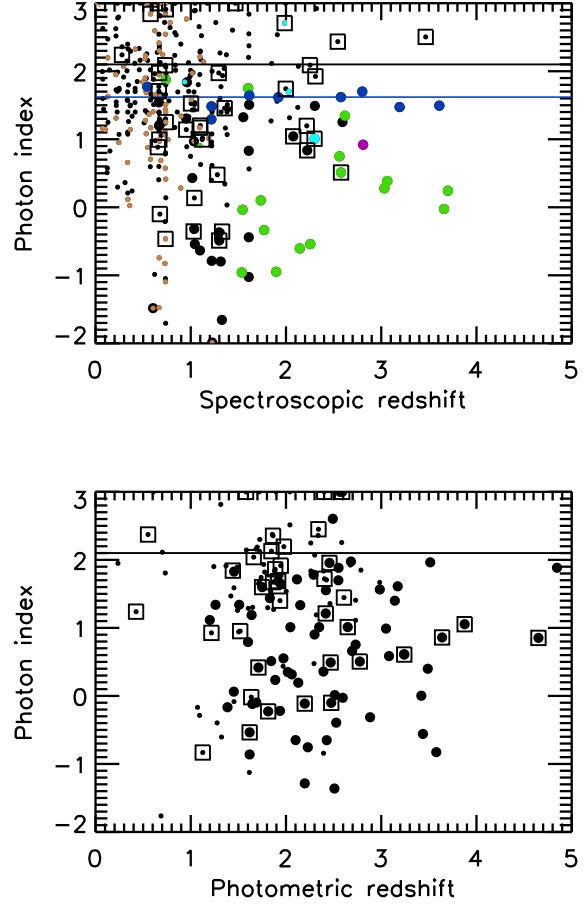


Figure 11. (a) Effective observed photon index from L17 vs. redshift for the central region X-ray sample with speczs. The blue line shows $\bar{\Gamma} = 1.62$ for the BLAGNs. The optical spectral classifications are color-coded (purple—BALQSO; blue—BLAGNs; green—Sy2s; black—SFGs; gold—Abs; cyan—no IDs). (b) The same, but for the central region X-ray sample with only photzs. There are no spectral classifications for these sources, so they are all shown as black. In both panels, sources with $L_{8-28\ \text{keV}}^R > 10^{42.5}\ \text{erg s}^{-1}$ are shown with larger symbols, sources with $> 3\sigma$ detections at $850\ \mu\text{m}$ are enclosed in open squares, and $\Gamma = 2.1 \pm 0.1$ for luminous, high-mass X-ray binaries from Sazonov & Khabibullin (2017) is indicated with the black line.

However, before drawing conclusions based on the above results, we need to consider the possibility that we may be better able to measure speczs in galaxies that are relatively unobscured and hence biased against submillimeter detections. To check this, we plot Γ versus photz for the central region X-ray sample with only photzs in Figure 11(b). There are 37 $> 3\sigma$ submillimeter sources out of 347 in the specz sample of Figure 11(a) ($10.7 \pm 1.7\%$) and 38 out of 160 in the photz sample

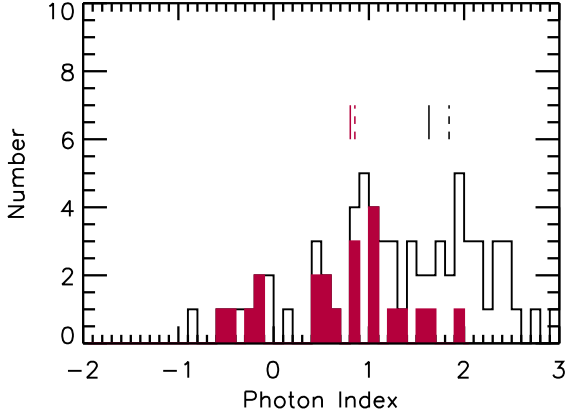


Figure 12. Effective observed photon index distribution for the central region X-ray sample with $> 3\sigma$ detections at $850\ \mu\text{m}$ split by luminosity: $L_{8-28\ \text{keV}}^R > 10^{42.5}\ \text{erg s}^{-1}$ (red shaded histogram) and lower X-ray luminosities (open histogram). The Γ are from L17. The means (solid lines) and medians (dashed lines) for the two samples are marked (red for the red shaded histogram, and black for the open histogram).

of Figure 11(b) ($24 \pm 4\%$), suggesting that submillimeter sources are indeed preferentially missed in the specz sample (see also Figure 4).

Since we do not have spectral classifications for the X-ray sources with only photzs, we can only use Γ and the estimated X-ray luminosity as diagnostics. However, we can see from Figure 11(b) that the population of submillimeter detected X-ray sources (enclosed in open squares) separates into a lower X-ray luminosity sample (smaller symbols) with mostly soft Γ , consistent with these sources being star formers, and a more X-ray luminous population (larger symbols) with mostly hard Γ . These latter sources correspond to the intermediate X-ray luminosity AGNs with submillimeter detections that we discussed in Section 3.3.

We can see this more clearly in Figure 12, where we show the Γ distribution for the submillimeter detected X-ray sources divided into sources with $L_{8-28\ \text{keV}}^R > 10^{42.5}\ \text{erg s}^{-1}$ (red shaded histogram) and those with lower X-ray luminosities (open histogram). While there is clearly a large spread in Γ for both X-ray luminosity samples, we find that the mean for the red shaded histogram sample ($\bar{\Gamma} = 0.55$) is significantly lower than the mean for the open histogram sample ($\bar{\Gamma} = 1.58$). These means are marked on the figure (solid lines), along with the medians (dashed lines). A Mann-Whitney test gives a one-sided probability of 10^{-5} that the two samples are drawn from the same distribution. As expected, this suggests that most of the red shaded histogram sources are dominated by highly absorbed AGN activity, while most of the open histogram sources are dominated by

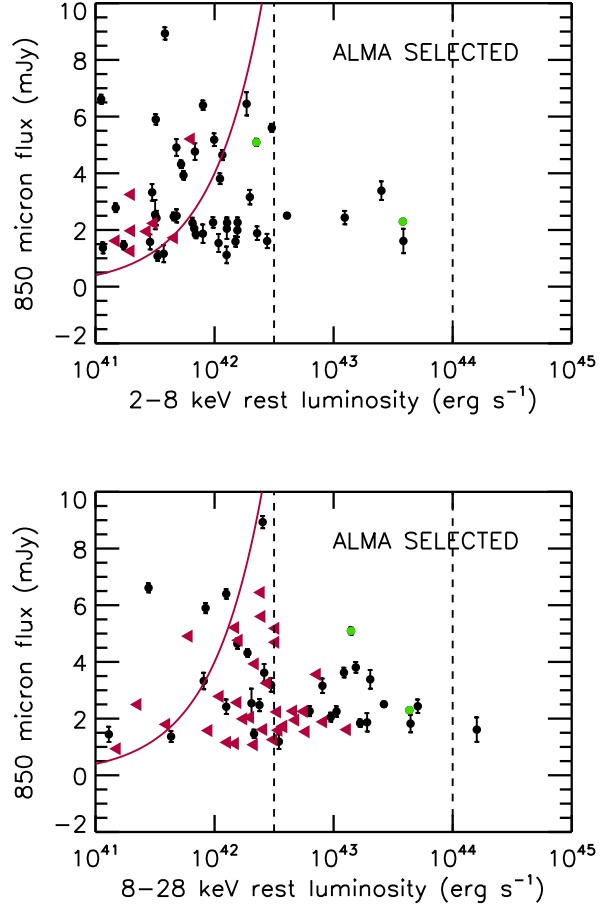


Figure 13. $850\ \mu\text{m}$ flux vs. (a) $L_{2-8\ \text{keV}}^R$ and (b) $L_{8-28\ \text{keV}}^R$ for the full ALMA sample (black circles). In both panels, green circles show Sy2s. No BLAGNs nor the BALQSO are present. Sources not detected at the $> 2\sigma$ level in (a) 0.5–2 keV and (b) 2–7 keV are shown with red left-pointing triangles at the 2σ X-ray luminosity in that band. For sources with measured X-ray luminosities, we show $\pm 1\sigma$ uncertainties in the submillimeter flux. The red curve shows the relation for sources where the X-rays are due to star formation. The dashed vertical lines show $10^{42.5}$ and $10^{44}\ \text{erg s}^{-1}$.

star formation activity; however, the latter sample also contains a small number of absorbed AGNs.

5. X-RAY PROPERTIES OF THE ALMA SAMPLE

We now turn to the X-ray properties of the ALMA sample. The ALMA sample allows us to probe more deeply in X-rays and to determine the fraction of submillimeter sources that do not have X-ray counterparts, even at the depths of the CDF-S 7 Ms image.

In Figure 13, we plot $850\ \mu\text{m}$ flux versus (a) $L_{2-8\ \text{keV}}^R$ and (b) $L_{8-28\ \text{keV}}^R$ for the full ALMA sample. The red curve shows the relation for sources where the X-rays are due to star formation (see Section 3.3). Clearly, the sub-

millimeter picks out both star formers and intermediate X-ray luminosity AGNs in the X-rays, but not the most luminous X-ray sources, which include the BLAGNs and many of the Sy2s.

More specifically, we can see that in Figure 13(a), all but five of the ALMA sources have low X-ray luminosities ($< 10^{42.5}$ erg s $^{-1}$). Intermediate X-ray luminosity AGNs, because of their high optical depths, are more easily seen in Figure 13(b). However, even for this 2–7 keV band, which has much poorer sensitivity, most of the sources are consistent with being star formation dominated, at least in as far as the upper limits are constraining. The ALMA sample picks out one high and 15 intermediate X-ray luminosity AGNs.

Finally, in Figure 14, we combine the two samples and plot (a), (c) $L_{2-8 \text{ keV}}^R$ and (b), (d) $L_{8-28 \text{ keV}}^R$ versus submillimeter flux for both the central X-ray (red) and ALMA (blue) samples; sources included in both samples are green. We show linear representations in the (a), (b) plots, since the X-ray luminosities and submillimeter fluxes may be negative, and these plots are helpful in visualizing the large number of low luminosity sources, but we also show the logarithmic versions in the (c), (d) plots to provide a clearer representation of the full range of X-ray luminosities. It is again evident that most of the ALMA sources (blue and green) are not very luminous in X-rays. For sources with 850 μ m fluxes above 2.25 mJy, only 10 of the 36 sources have $L_{8-28 \text{ keV}}^R > 10^{42.5}$ erg s $^{-1}$, while above 4 mJy, only 1 of the 11 sources does.

In Figures 14(c), (d), the black curve shows the relation for the sources where the X-rays are due to star formation. Most of the ALMA sources, both with (green) and without (blue) X-ray detections, appear to be consistent with having both their X-ray and their submillimeter emission driven by star formation, even for the harder $L_{8-28 \text{ keV}}^R$. However, a small population of ALMA sources with intermediate X-ray luminosities is only clearly seen in Figures 14(b), (d), reflecting their high obscuration (see Section 4).

6. DISCUSSION

In order to search for variance and to increase the size of the sample for statistical analyses, we now combine the CDF-S with the CDF-N, where we have the 2 Ms X-ray image from Alexander et al. (2003) and the submillimeter data (SCUBA-2 and SMA) from C17. In Figure 15, we show submillimeter flux versus $L_{8-28 \text{ keV}}^R$ for $z = 1.5$ – 4.5 (specz and photz) sources in the CDF-S (black circles) and CDF-N (red squares) lying at off-axis angles $< 8'$, where the rms noise is < 1 mJy for all sources. We will hereafter refer to this as the *combined X-ray sample*.

Both fields have a number of strong submillimeter sources (850 μ m fluxes > 2.25 mJy, black line) at intermediate X-ray luminosities powered by AGNs (gold shaded region; hereafter, we refer to these sources as

submillimeter AGNs), but not at high X-ray luminosities. Indeed, the distributions of the submillimeter fluxes are significantly different: a Mann-Whitney test gives only a 4% probability that sources just below the highest X-ray luminosities (namely, $L_{8-28 \text{ keV}}^R = 10^{43.5}$ – 10^{44} erg s $^{-1}$) are drawn from the same distribution as sources at $L_{8-28 \text{ keV}}^R > 10^{44}$ erg s $^{-1}$.

We note that Page et al. (2012) found a similar result using low resolution and much shorter wavelength *Herschel*-SPIRE 250 μ m data on only the CDF-N. Based on a combined *Herschel*-SPIRE 250 μ m data sample from the CDF-N, CDF-S, and COSMOS, Harrison et al. (2012) argued that the Page et al. result was likely a consequence of poor source statistics and potentially cosmic variance. We emphasize that ultimately much larger samples will be required to provide very robust results.

A Kolmogorov-Smirnov test shows that the submillimeter fluxes for X-ray sources in the range $L_{8-28 \text{ keV}}^R = 10^{43}$ – 10^{44} erg s $^{-1}$ have a $< 1\%$ probability of being normally distributed. They have a mean flux of 1.00 mJy with a 95% confidence range 0.59–1.42 mJy. In contrast, the submillimeter fluxes for X-ray sources at $L_{8-28 \text{ keV}}^R > 10^{44}$ erg s $^{-1}$ are consistent with being normally distributed (probability of 0.31). They have a mean flux of 0.58 mJy with a 95% confidence range 0.19–0.98 mJy. This corresponds to a drop in the mean SFR from the intermediate to the high X-ray luminosity range of $\sim 140 M_\odot \text{ yr}^{-1}$ to $\sim 80 M_\odot \text{ yr}^{-1}$.

As discussed in Section 4, the submillimeter AGNs correspond to sources with high absorption in their X-ray spectra. In Figure 16(a), we show X-ray absorption column density, N_H , versus $L_{8-28 \text{ keV}}^R$ for the combined X-ray sample. We calculate N_H by assuming the intrinsic power law is 1.8 and then comparing with the individual effective observed Γ values from L17. We show the strong submillimeter sources with large red circles. We also show sources spectrally classified as BLAGNs (blue circles) or Sy2s (green circles). There are a small number of submm AGNs that have a BLAGN or Sy2 spectral classification, which we denote by red circles with blue or green interiors, respectively. (Note that the only BLAGN in this category comes from the CDF-N.)

As we discussed in Section 2.7 and stressed in Section 3.3, we have not corrected the X-ray luminosities for any intrinsic absorption. For high redshifts, the 2–7 keV band corresponds to very high energies, so these corrections are small. We use N_H to calculate the absorption corrections in each of the energy bands. We show N_H versus absorption-corrected $L_{8-28 \text{ keV}}^R$ in Figure 16(b). We can see the effect is very minor, moving the high N_H sources to slightly higher luminosities relative to the lower N_H sources.

We see that the submm AGNs primarily have high N_H , while the Sy2s lie, on average, at higher X-ray luminosities but still have high N_H , and the BLAGNs lie

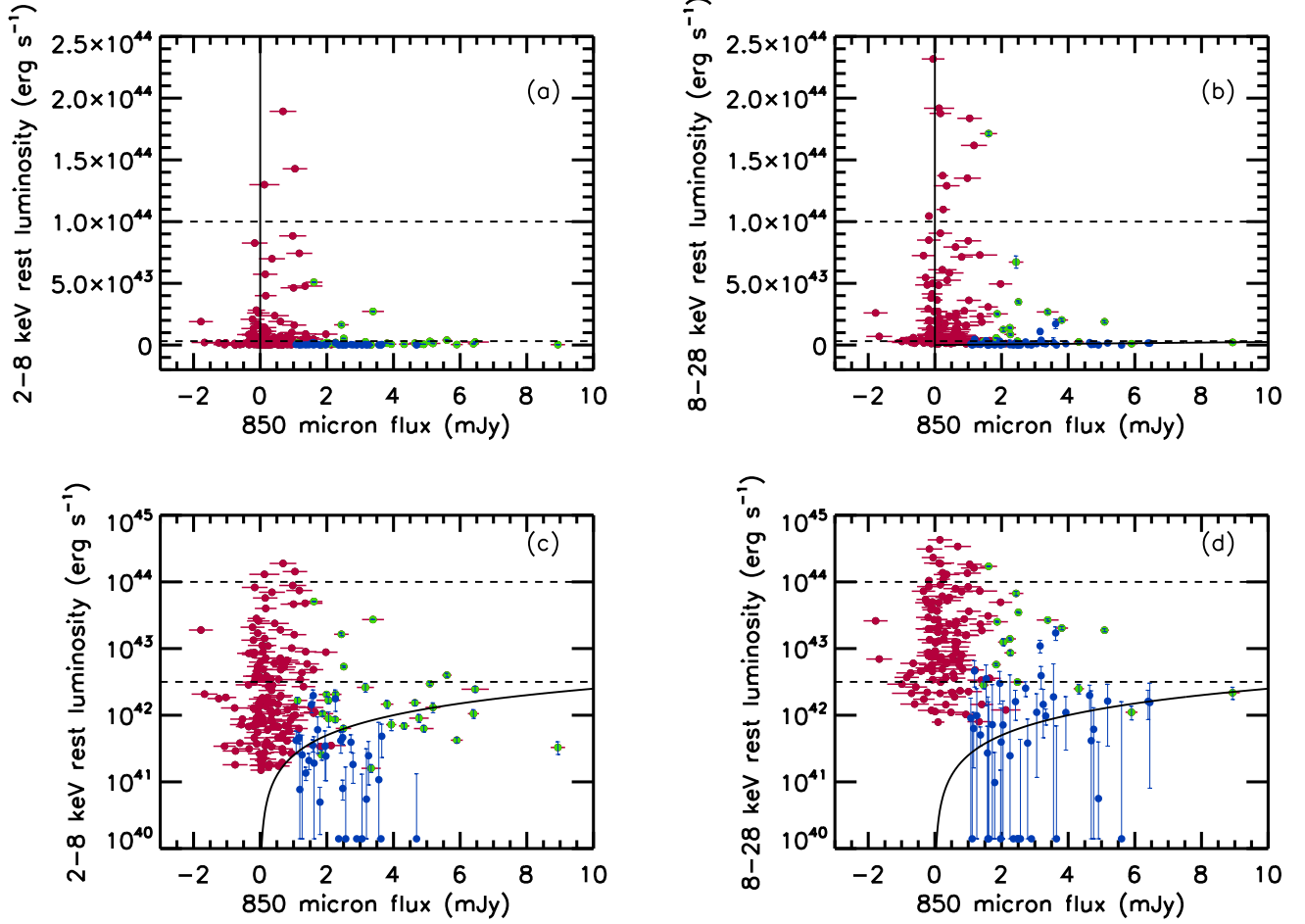


Figure 14. (a), (b) Linear and (c), (d) logarithmic representations of (a), (c) $L_{2-8 \text{ keV}}^R$ and (b), (d) $L_{8-28 \text{ keV}}^R$ vs. $850 \mu\text{m}$ flux in the central region, restricted to sources with $1 < z < 4.5$; the upper cut-off is to avoid the highly uncertain photzs of high-redshift candidates (see Cowie et al. 2019). $L_{2-8 \text{ keV}}^R$ or $L_{8-28 \text{ keV}}^R < 10^{40} \text{ erg s}^{-1}$ sources are placed at $\sim 10^{40} \text{ erg s}^{-1}$. Red circles show sources from the X-ray sample ((a), (c), restricted to 0.5–2 keV fluxes above $2 \times 10^{-17} \text{ erg cm}^{-2} \text{ s}^{-1}$, and (b), (d), restricted to 2–7 keV fluxes above $10^{-16} \text{ erg cm}^{-2} \text{ s}^{-1}$), blue from the ALMA sample (note that the X-ray luminosities are based on the redshifts given in Table 2, and photzs for submillimeter sources can be quite uncertain; see C18), and green are present in both. We show $\pm 1\sigma$ uncertainties in the $850 \mu\text{m}$ flux for the X-ray sources, and $\pm 1\sigma$ uncertainties in the X-ray luminosity for the submillimeter sources. In (c) and (d), the black curve shows the relation for sources where the X-rays are due to star formation. The dashed horizontal lines show $10^{42.5}$ and $10^{44} \text{ erg s}^{-1}$.

at the highest X-ray luminosities but have lower N_H . We schematically illustrate this in Figure 16(c).

It is plausible to interpret this result in terms of the Sanders-Hopkins merger model (Sanders et al. 1988; Hopkins et al. 2006). After the early stages of the merger process, an intense star formation period occurs (hundreds of solar masses per year), which we would identify with the strong submillimeter sources. This is followed by declining star formation and high X-ray luminosity, which we would identify with the Sy2 population. Then, as the gas is cleared from the system but the X-ray luminosity remains high, we would identify the source as a BLAGN. The timescales of each episode are comparable in this interpretation so that we would expect to

see similar numbers of sources in each stage, as is indeed the case.

7. SUMMARY

We used the X-ray catalog of L17 for the CDF-S to construct a full X-ray sample of 938 sources (off-axis angles $< 10'$) complemented with SCUBA-2 $850 \mu\text{m}$ data with noise $< 1.5 \text{ mJy}$ (C18). We also constructed a central region X-ray sample of 526 sources (off-axis angles $< 5'.7$) complemented with SCUBA-2 $850 \mu\text{m}$ data with noise $< 0.56 \text{ mJy}$ (this corresponds to a 4σ limit of $> 2.25 \text{ mJy}$) and deep ALMA band 7 data (75 sources at $> 4.5\sigma$; C18).

We assigned secure specz to 64.5% of the sources in the full X-ray sample and spectral classifications to 64%.

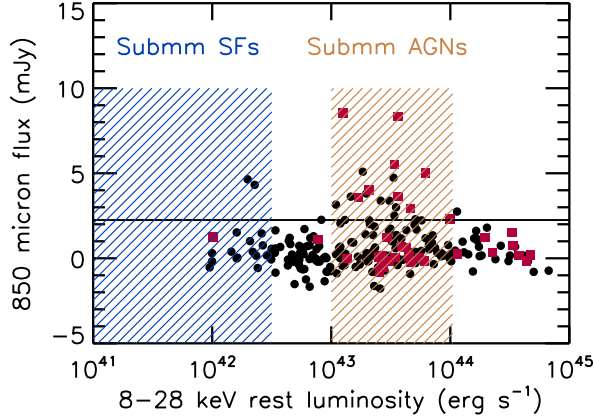


Figure 15. $850\ \mu\text{m}$ flux vs. $L_{8-28\ \text{keV}}^R$ for $z = 1.5-4.5$ (specz and photz) sources in the CDF-S (black circles) and CDF-N (red squares) lying at off-axis angles $< 8'$, where the rms noise is $< 1\ \text{mJy}$ for all sources. The black horizontal line shows a submillimeter flux of $2.25\ \text{mJy}$ ($322\ M_{\odot}\ \text{yr}^{-1}$), which roughly corresponds to the SCUBA-2 $> 4\sigma$ limit through the whole central region. We consider sources above this to be strong submillimeter sources. The blue shaded region shows where strong submillimeter sources are found for X-ray luminosities powered by star formation, and the gold shaded region shows where strong submillimeter sources are found for X-ray luminosities powered by AGNs.

However, for the $> 3\sigma$ submillimeter detected X-ray sources, the percentage of speczs is much smaller (50%), likely due to the fact that these sources are dustier, fainter in the optical/NIR, and at higher redshifts. After including photzs from the literature (H14 and S16), all but 44 of the sources in the full X-ray sample have a redshift. Most of the X-ray sources lie at low redshifts (58% at $z < 1.6$, 88% of which are speczs), while only a handful lie at high redshifts (9 sources at $z > 4$ and 2 sources at $z > 5$, nearly all of which are photzs; see Cowie et al. 2019 for a detailed discussion of these very high-redshift AGN candidates).

We presented a catalog of the X-ray and submillimeter properties, redshifts, and spectral classes of the full X-ray sample. We also presented a catalog of the X-ray properties and redshifts of the 75 ALMA sources.

Our major results are as follows:

- Most of the spectrally classified X-ray sources with $> 3\sigma$ $850\ \mu\text{m}$ detections are star-forming galaxies; very few Sy2s and no BLAGNs in either the full or central X-ray samples have $850\ \mu\text{m}$ detections at $> 3\sigma$.
- The X-ray sources contain a significant $850\ \mu\text{m}$ flux with a mean of $0.52\ \text{mJy}$ per X-ray source with a 95% confidence range of 0.44 to $0.61\ \text{mJy}$.

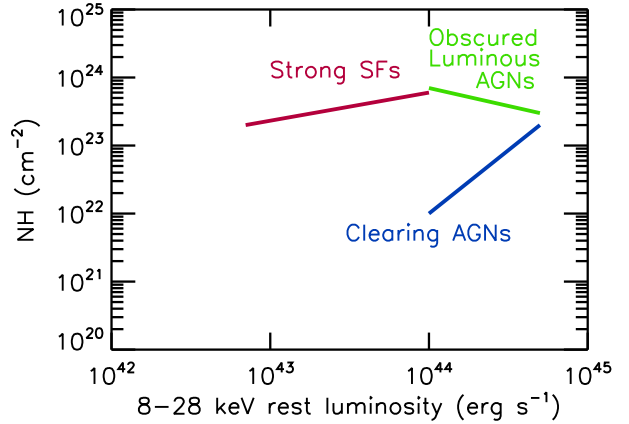
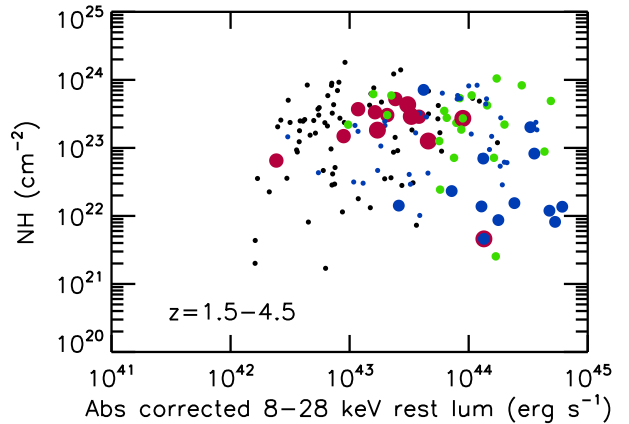
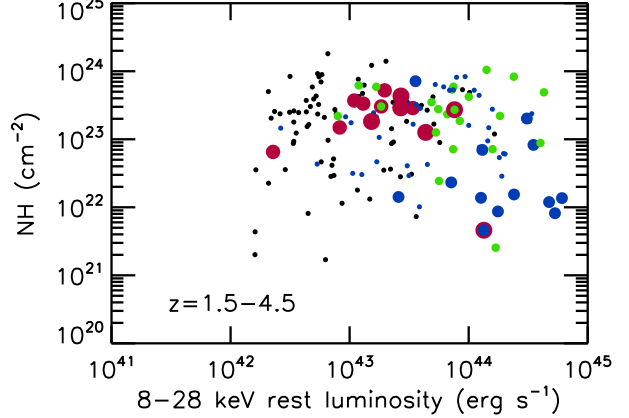


Figure 16. X-ray absorption column density, N_H , vs. (a) $L_{8-28\ \text{keV}}^R$ and (b) absorption-corrected $L_{8-28\ \text{keV}}^R$ for $z = 1.5-4.5$ (specz and photz) sources in the CDF-S and CDF-N lying at off-axis angles $< 8'$, where the rms noise is $< 1\ \text{mJy}$ for all sources. Strong submillimeter sources ($> 2.25\ \text{mJy}$, or $> 322\ M_{\odot}\ \text{yr}^{-1}$) are shown with red circles. Spectrally classified BLAGNs are shown in blue, and Sy2s in green. Sources that are both a strong submillimeter source and have a BLAGN or Sy2 spectral classification are shown as red circles with blue or green interiors, respectively. The only BLAGN in this category comes from the CDF-N. (c) Schematic outline with the location of the various stages labeled.

However, nearly all of the signal comes from those X-ray sources that are significantly detected in the submillimeter. The bulk of the X-ray sources are consistent with having no 850 μm flux. This emphasizes the dangers of using simple stacking analyses on samples where the sources producing most of the 850 μm flux lie in a very extended tail.

- Only $\sim 10\%$ of the 850 μm EBL measured by Fixsen et al. (1998) is identified by X-ray sources (sources where the X-ray emission is powered by AGNs and sources where the X-ray emission is powered by star formation) at the limits of the *Chandra* 7 Ms data. Thus, Compton-thin X-ray detected AGNs, which we are sensitive to out to $z \sim 6$, do not mark the galaxies responsible for producing most of the 850 μm light.
- Our analysis uses X-ray luminosities uncorrected for absorption (except in the Discussion), but for high redshifts, the 2–7 keV band corresponds to very high energies, so these corrections are small. The brightest 850 μm detected X-ray sources are primarily at low X-ray luminosities ($L_{8-28 \text{ keV}}^R < 10^{42.5} \text{ erg s}^{-1}$). In fact, all but one of the central region X-ray sources with an 850 μm flux $> 4 \text{ mJy}$ are consistent with both the X-ray luminosity and the 850 μm flux being produced by star formation.
- At X-ray luminosities that can only be produced by an AGN ($L_{8-28 \text{ keV}}^R > 10^{42.5} \text{ erg s}^{-1}$), only 8 sources are strong submillimeter sources (850 μm flux $> 2.25 \text{ mJy}$), all of which are at intermediate X-ray luminosities ($10^{42.5} < L_{8-28 \text{ keV}}^R < 10^{44} \text{ erg s}^{-1}$). Thus, it appears that extreme SFRs $\gtrsim 300 \text{ M}_{\odot} \text{ yr}^{-1}$ are only seen in the hosts of intermediate X-ray luminosity AGNs.
- Consistent with the above results, the distribution of the effective observed photon indices for the 850 μm detected $L_{8-28 \text{ keV}}^R > 10^{42.5} \text{ erg s}^{-1}$ sources ($\bar{\Gamma} = 0.55$) is significantly different than the distribution for the 850 μm detected lower X-ray luminosity sources ($\bar{\Gamma} = 1.58$); this suggests that the former are dominated by highly absorbed AGN activity, while the latter are dominated by star formation activity.
- Starting with the ALMA sample makes it possible to probe the X-ray data more deeply. Most of the ALMA sources appear to be consistent with having both their X-ray and their 850 μm emission

driven by star formation, with only a small population having intermediate X-ray luminosities.

- Our results are consistent with seeing the effects of gas being cleared and the SFR being lowered as the galaxy becomes more transparent and X-ray luminous.

We thank the anonymous referee for a careful report that helped us to improve the manuscript. We gratefully acknowledge support from NSF grant AST-1313150 (A. J. B.), NASA grant NNX17AF45G (L. L. C.), CONICYT grants Basal-CATA PFB-06/2007 (F. E. B., J. G.-L.) and Programa de Astronomía FONDO ALMA 2016 31160033 (J. G.-L.), and the Ministry of Economy, Development, and Tourism’s Millennium Science Initiative through grant IC120009, awarded to The Millennium Institute of Astrophysics, MAS (F. E. B.). Este trabajo contó con el apoyo de CONICYT + Programa de Astronomía + Fondo CHINA-CONICYT CAS16026 (J. G.-L.). Support for this research was also provided by the University of Wisconsin-Madison, Office of the Vice Chancellor for Research and Graduate Education with funding from the Wisconsin Alumni Research Foundation, the John Simon Memorial Guggenheim Foundation, and the Trustees of the William F. Vilas Estate (A. J. B.). A. J. B. would like to thank the Lorentz Center for the stimulating workshop “Monsters of the Universe: The Most Extreme Star Factories” that benefited this work. ALMA is a partnership of ESO (representing its member states), NSF (USA) and NINS (Japan), together with NRC (Canada), MOST and ASIAA (Taiwan), and KASI (Republic of Korea), in cooperation with the Republic of Chile. The Joint ALMA Observatory is operated by ESO, AUI/NRAO and NAOJ. The James Clerk Maxwell Telescope is operated by the East Asian Observatory on behalf of The National Astronomical Observatory of Japan, Academia Sinica Institute of Astronomy and Astrophysics, the Korea Astronomy and Space Science Institute, the National Astronomical Observatories of China and the Chinese Academy of Sciences (Grant No. XDB09000000), with additional funding support from the Science and Technology Facilities Council of the United Kingdom and participating universities in the United Kingdom and Canada. The W. M. Keck Observatory is operated as a scientific partnership among the California Institute of Technology, the University of California, and NASA, and was made possible by the generous financial support of the W. M. Keck Foundation. The authors wish to recognize and acknowledge the very significant cultural role and reverence that the summit of Maunakea has always had within the indigenous Hawaiian community. We are most fortunate to have the opportunity to conduct observations from this mountain.

REFERENCES

- Alexander, D. M., Bauer, F. E., Brandt, W. N., et al. 2003, *AJ*, 126, 539
- Ashby, M. L. N., Willner, S. P., Fazio, G. G., et al. 2013, *ApJ*, 769, 80

- Balestra, I., Mainieri, V., Popesso, P., et al. 2010, *A&A*, 512, 12
- Barger, A. J., Cowie, L. L., Owen, F., et al. 2015, *ApJ*, 801, 87
- Barger, A. J., Cowie, L. L., Steffen, A. T., et al. 2001, *ApJ*, 560, L23
- Blain, A. W., & Longair, M. S. 1993, *MNRAS*, 264, 509
- Casey, C. M., Chapman, S. C., Smail, I., et al. 2011, *MNRAS*, 411, 2739
- Cooper, M. C., Yan, R., Dickinson, M., et al. 2012, *MNRAS*, 425, 2116
- Cowie, L. L., Barger, A. J., Bauer, F. E., & González-López, J. 2020, *ApJ*, in press
- Cowie, L. L., Barger, A. J., & Hasinger, G. 2012, *ApJ*, 748, 50
- Cowie, L. L., Barger, A. J., Hsu, L.-Y., et al. 2017, *ApJ*, 837, 139 (C17)
- Cowie, L. L., Barger, A. J., & Songaila, A. 2016, *ApJ*, 817, 57
- Cowie, L. L., González-López, J., Barger, A. J., et al. 2018, *ApJ*, 865, 106 (C18)
- Cowie, L. L., Songaila, A., Hu, E. M., & Cohen, J. G. 1996, *AJ*, 112, 839
- Dahlen, T., Mobasher, B., Faber, S. M., et al. 2013, *ApJ*, 775, 93
- Dunlop, J. S., McLure, R. J., Biggs, A. D., et al. 2017, *MNRAS*, 466, 861
- Faber, S. M., Phillips, A. C., Kibrick, R. I., et al. 2003, *SPIE*, 4841, 1657
- Fixsen, D. J., Dwek, E., Mather, J. C., Bennett, C. L., & Shafer, R. A. 1998, *ApJ*, 508, 123
- Franco, M., Elbaz, D., Béthermin, M., et al. 2018, *A&A*, 620, A152
- Harrison, C. M., Alexander, D. M., Mullaney, J. R., et al. 2012, *ApJ*, 760, L15
- Hatziminaoglou, E., Omont, A., Stevens, J. A., et al. 2010, *A&A*, 518, L33
- Hodge, J. A., Karim, A., Smail, I., et al. 2013, *ApJ*, 768, 91
- Hopkins, P. F., Hernquist, L., Cox, T. J., et al. 2006, *ApJS*, 163, 1
- Hsieh, B.-C., Wang, W.-H., Hsieh, C.-C., et al. 2012, *ApJS*, 203, 23
- Hsu, L.-T., Salvato, M., Nandra, K., et al. 2014, *ApJ*, 796, 60 (H14)
- Inami, H., Bacon, R., Brinchmann, J., et al. 2017, *A&A*, 608, A2
- Kriek, M., Shapley, A. E., Reddy, N. A., et al. 2015, *ApJS*, 218, 15
- Kroupa, P. 2001, *MNRAS*, 322, 231
- Kurk, J., Cimatti, A., Daddi, E., et al. 2013, *A&A*, 549, 63
- Labbé, I., Oesch, P. A., Illingworth, G. D., et al. 2015, *ApJS*, 221, 23
- Lehmer, B. D., Xue, Y. Q., Brandt, W. N., et al. 2012, *ApJ*, 752, 46
- Le Fèvre, O., Vettolani, G., Garrili, B., et al. 2005, *A&A*, 439, 845
- Luo, B., Brandt, W. N., Xue, Y. Q., et al. 2017, *ApJS*, 228, 2 (L17)
- Lutz, D., Mainieri, V., Rafferty, D., et al. 2010, *ApJ*, 712, 1287
- McLean, I. S., Steidel, C. C., Epps, H. W., et al. 2012, *SPIE*, 8446, 84460J
- McLure, R. J., Pentericci, L., Cimatti, A., et al. 2018, *MNRAS*, 479, 25
- Mignoli, M., Cimatti, Z., Zamorani, G., et al. 2005, *A&A*, 437, 883
- Mineo, S., Gilfanov, M., & Sunyaev, R. 2012, *MNRAS*, 419, 2095
- Morris, A. M., Kocevski, D. D., Trump, J. R., et al. 2015, *AJ*, 149, 178
- Mullaney, J. R., Alexander, D. M., Aird, J., et al. 2015, *MNRAS*, 453, L83
- Nguyen, H. T., Schulz, B., Levenson, L., et al. 2010, *A&A*, 518, L5
- Oke, J. B., Cohen, J. G., Carr, M., et al. 1995, *PASP*, 107, 375
- Page, M. J., Symeonidis, M., Vieira, J. D., et al. 2012, *Natur*, 485, 213
- Popesso, P., Dickinson, M., Nonino, M., et al. 2009, *A&A*, 494, 443
- Rafferty, D. A., Brandt, W. N., Alexander, D. M., et al. 2011, *ApJ*, 742, 3
- Ramasawmy, J., Stevens, J., Martin, G., Geach, J. E. 2019, *MNRAS*, 486, 4320
- Rosario, D. J., Santini, P., Lutz, D., et al. 2012, *A&A*, 545, A45
- Sanders, D. B., Soifer, B. T., Elias, J. H., et al. 1988, *ApJ*, 325, 74
- Santini, P., Ferguson, H. C., Fontana, A., et al. 2015, *ApJ*, 801, 97
- Santini, P., Fontana, A., Grazian, A., et al. 2009, *A&A*, 504, 751
- Sazonov, S., & Khabibullin, I. 2017, *MNRAS*, 468, 2249
- Scholtz, J., Alexander, D. M., Harrison, C. M., et al. 2018, *MNRAS*, 475, 1288
- Schreiber, C. Pannella, M., Leiton, R., et al. 2017, *A&A*, 599, A134
- Shao, L., Lutz, D., Nordon, R., et al. 2010, *A&A*, 518, L26
- Silverman, J. D., Mainieri, V., Salvato, M., et al. 2010, *ApJS*, 191, 124
- Skelton, R. E., Whitaker, K. E., Momcheva, I. G., et al. 2014, *ApJS*, 214, 24
- Straatman, C. M. S., Spitler, L. R., Quadri, R. F., et al. 2016, *ApJ*, 830, 51 (S16)
- Stanley, F., Harrison, C. M., Alexander, D. M., et al. 2015, *MNRAS*, 453, 591
- Stanley, F., Harrison, C. M., Alexander, D. M., et al. 2018, *MNRAS*, 478, 3721
- Szokoly, G. P., Bergeron, J., Hasinger, G., et al. 2004, *ApJS*, 155, 271
- Ueda, Y., Hatsukade, B., Kohno, K., et al. 2018, *ApJ*, 853, 24
- Urrutia, T., Wisotzki, L., Kerutt, J., et al. 2019, *A&A*, 624, A141
- Vanzella, E., Cristiani, S., Dickinson, M., et al. 2008, *A&A*, 478, 83
- Xue, Y. Q., Luo, B., Brandt, W. N., et al. 2011, *ApJS*, 195, 10
- Zavala, J. A., Aretxaga, I., Geach, J. E., et al. 2017, *MNRAS*, 464, 3369

Table 1. X-ray and Submillimeter Properties, Redshifts, and Spectral Classes of the Full X-ray Sample

L17 No.	R.A. J2000.0 (1)	Decl. J2000.0 (3)	$f_{0.5-2 \text{ keV}}$ ($10^{-17} \text{ erg cm}^{-2} \text{ s}^{-1}$) (4)	$f_{2-7 \text{ keV}}$ (5)	$f_{850 \mu\text{m}}$ (mJy) (6)	Error (7)	ALMA Flag (8)	z_{spec} (9)	Spectral Class (10)	Reference (11)	z_{phot} (12)
518	53.118004	-27.802055	1.96	-1.07	-0.45	0.25	0	0.000	Star	aqp	0.446
487	53.111496	-27.802973	1.21	-3.24	0.068	0.25	0		0.732
530	53.120167	-27.798832	2.20	-2.88	1.0	0.26	0		2.340
482	53.110790	-27.800556	1.18	-4.90	.0086	0.15	1		2.731
491	53.111706	-27.813999	1.25	-2.64	0.021	0.25	0		2.585
470	53.108250	-27.797583	3.17	-2.29	0.065	0.17	1		1.895
575	53.128834	-27.813749	-0.586	6.84	0.56	0.26	0		2.394
442	53.103870	-27.804028	1.33	-2.65	-0.36	0.21	0	0.128	Abs	q	0.144
578	53.129749	-27.799028	0.774	-4.88	0.36	0.26	0		2.731
531	53.120750	-27.818972	1.68	-8.06	1.4	0.26	0	1.094	Abs	abh	1.075
589	53.131332	-27.814917	11.5	16.1	1.2	0.27	0		1.917
432	53.102543	-27.814278	1.47	-4.99	0.75	0.25	0	0.577	SFR	adp	...
598	53.134293	-27.812611	1.67	-4.10	0.20	0.27	0	0.535	SFR	aqph	0.525
478	53.110081	-27.791750	-0.892	5.35	0.035	0.26	0
426	53.099918	-27.808416	1.06	7.44	0.38	0.25	0		1.969
431	53.102543	-27.814278	2.41	3.47	0.70	0.25	0	0.579	SFR	adp	0.484
477	53.109539	-27.820805	2.42	7.49	0.30	0.25	0	0.338	SFR	ah	0.331
533	53.120834	-27.823055	-1.23	13.2	0.89	0.26	0	0.735	Abs	bp	0.741
616	53.137749	-27.802084	2.69	9.00	0.13	0.28	0	1.188	Abs	qh	1.202
580	53.130417	-27.791054	5.37	29.9	0.093	0.28	0		3.240
481	53.110580	-27.823610	3.52	-2.26	0.86	0.26	0	1.468	SFR	abh	1.415
604	53.136333	-27.816528	1.25	-2.22	0.094	0.28	0	0.670	SFR	dh	0.667
583	53.130627	-27.790222	3.19	-3.32	0.11	0.28	0	0.666	SFR	aqeh	0.677
609	53.137165	-27.815638	0.884	-2.29	0.34	0.28	0	0.837	SFR	ah	0.838
417	53.097248	-27.814554	3.76	4.85	0.33	0.25	0	0.248	SFR	adeh	0.248
537	53.121712	-27.785418	2.51	-3.51	0.36	0.28	0	0.669	Abs	abqef	0.676
508	53.115498	-27.827055	-0.956	-5.95	-0.46	0.27	0	0.227	SFR	ah	...
401	53.094086	-27.804167	2.04	46.2	1.8	0.13	1	1.299	SFR	b	2.391
429	53.101501	-27.821556	1.42	-3.85	-0.32	0.26	0		2.425

NOTE— Excerpt of full table, which is available in its entirety in machine-readable form in the journal. The table is ordered by *Chandra* off-axis angle, such that the 526 sources in the central region X-ray sample appear first, extending down to source L17 #492. The columns are (1) X-ray source number from L17, (2) and (3) optical/NIR R.A. and Decl., (4) and (5) observed 0.5–2 keV and 2–7 keV fluxes, (6) and (7) observed 850 μm flux and error, (8) a “1” if the submillimeter flux measurement is based on ALMA data and a “0” if it is based on SCUBA-2 data, (9) specz, (10) spectral class, (11) reference for the spectra used in the spectral classification (a=our Keck DEIMOS, b=Vanzella et al. 2008, c,d=Balestra et al. 2010, e=Szokoly et al. 2004, f=Silverman et al. 2010, g=Kurk et al. 2013, h=Inami et al. 2017, Urrutia et al. 2019, i=McLure et al. 2018, j=our Keck MOSFIRE, k=Kriek et al. 2015, l=our Keck LRIS, m=Casey et al. 2011, n=Morris et al. 2015, o=Cooper et al. 2012, p=Le Fèvre et al. 2005, q=Mignoli et al. 2005), and (12) photz from H14, or, if there is no photz in H14, then from S16.

Table 2. X-ray Properties and Redshifts of the 850 μm ALMA Sample from C18

C18	L17	R.A.	Decl.	$f_{850\mu\text{m}}$	Error	$f_{0.5-2\text{keV}}$	Error	$f_{2-7\text{keV}}$	Error	z_{spec}	z_{phot}
No.	No.	J2000.0	J2000.0	(mJy)		($10^{-17}\text{ erg cm}^{-2}\text{ s}^{-1}$)		($10^{-17}\text{ erg cm}^{-2}\text{ s}^{-1}$)			
(1)	(2)	(3)	(4)	(5)	(6)	(7)	(8)	(9)	(10)	(11)	(12)
1	162	53.030373	-27.855804	8.93	0.21	2.73	0.58	18.1	3.78	...	[3.28]
2	...	53.047211	-27.870001	8.83	0.26	4.45
3	276	53.063877	-27.843779	6.61	0.16	14.9	0.35	37.3	2.08	...	3.12
4	132	53.020374	-27.779917	6.45	0.41	5.86	0.61	3.86	3.66	2.252	1.95
5	522	53.118790	-27.782888	6.39	0.16	2.38	0.35	3.79	1.77	2.309	2.29
6	844	53.195126	-27.855804	5.90	0.18	4.94	0.48	12.9	3.03	...	[3.13]
7	714	53.158371	-27.733612	5.60	0.14	7.06	0.47	0.0331	2.91	...	3.48
8	453	53.105247	-27.875195	5.18	0.22	2.28	0.39	2.89	2.28	...	2.69
9	666	53.148876	-27.821167	5.09	0.12	5.30	0.33	33.6	1.74	2.576	2.55
10	353	53.082085	-27.767279	4.90	0.29	2.93	0.31	0.283	1.72	...	2.41
11	342	53.079376	-27.870806	4.76	0.29	3.25	0.44	2.37	2.61	...	[3.33]
12	640	53.142792	-27.827888	4.73	0.16	2.81	0.33	4.74	1.68	...	3.76
13	...	53.074837	-27.875916	4.69	0.81	-0.349	0.56	0.666	3.05	...	[3.68]
14	391	53.092335	-27.826834	4.64	0.17	3.18	0.31	4.25	1.77	...	2.73
15	140	53.024292	-27.805695	3.93	0.15	2.54	0.48	4.12	2.99	...	2.14
16	356	53.082752	-27.866585	4.31	0.15	3.91	0.41	14.1	2.34	...	3.37
17	657	53.146629	-27.871029	3.80	0.18	2.86	0.38	39.5	2.25	...	3.57
18	...	53.092834	-27.801332	5.21	0.32	0.645	0.33	-0.780	1.70	3.847	2.96
19	472	53.108795	-27.869028	3.62	0.17	-1.51	0.36	9.12	2.09	...	[6.69]
20	852	53.198292	-27.747889	3.61	0.30	-3.79	0.58	11.4	3.64	...	1.93
21	...	53.178333	-27.870222	3.55	0.20	0.0829	0.51	1.44	3.08	...	3.78
22	805	53.183460	-27.776638	3.38	0.32	54.0	0.36	53.1	2.13	2.698	2.86
23	710	53.157207	-27.833500	3.32	0.29	2.30	0.32	6.26	1.68	...	1.58
24	...	53.102791	-27.892860	3.25	0.14	0.842	0.53	4.94	3.37	...	1.96
25	...	53.181377	-27.777557	3.18	0.23	0.0756	0.35	5.40	2.00	2.794	2.92
26	299	53.070251	-27.845612	3.15	0.25	2.26	0.34	9.20	1.98	...	3.78
27	...	53.014584	-27.844389	3.05	0.19	0.0929	0.65	4.74	4.24	...	[4.60]
28	622	53.139290	-27.890722	2.89	0.37	1.38	0.50	1.25	3.20	...	[3.59]
29	...	53.137127	-27.761389	2.82	0.28	1.23	0.31	3.50	1.69
30	...	53.071709	-27.843693	2.78	0.15	0.703	0.33	1.47	1.89	...	1.86
31	...	53.077377	-27.859612	2.54	0.43	1.36	0.40	8.80	2.21	...	1.95
32	...	53.049751	-27.770971	2.56	0.16	-0.187	0.45	-1.83	2.52	...	2.75
33	313	53.072708	-27.834278	2.49	0.23	3.29	0.33	-1.90	1.72	...	1.58
34	386	53.090752	-27.782473	2.47	0.21	1.00	0.33	34.9	1.65	...	1.95

Table 2 continued

Table 2 (continued)

C18 No.	L17 No.	R.A. J2000.0	Decl. J2000.0	$f_{850\mu m}$ (mJy)	Error (6)	$f_{0.5-2\text{ keV}}$ (10^{-17} erg cm $^{-2}$ s $^{-1}$)	Error (8)	$f_{2-7\text{ keV}}$ (10^{-17} erg cm $^{-2}$ s $^{-1}$)	Error (10)	z_{spec} (11)	z_{phot} (12)
(1)	(2)	(3)	(4)	(5)	(6)	(7)	(8)	(9)	(10)	(11)	(12)
35	389	53.091747	-27.712166	2.47	0.13	2.97	0.65	-4.38	4.34	1.612	1.71
36	...	53.086586	-27.810249	2.41	0.25	0.913	0.32	3.52	1.67	...	2.37
37	...	53.146378	-27.888807	2.35	0.28	5.71	0.50	46.6	3.15	...	2.96
38	393	53.092335	-27.803223	2.50	0.10	10.5	0.33	68.5	1.70	...	2.31
39	...	53.124332	-27.882696	2.26	0.18	1.61	0.45	2.37	2.61	...	0.766
40	587	53.131123	-27.773195	2.26	0.17	5.06	0.34	21.2	1.72	2.224	2.22
41	...	53.172832	-27.858860	2.25	0.18	1.12	0.39	0.156	2.39
42	387	53.091629	-27.853390	2.25	0.18	3.30	0.34	53.5	1.87	...	2.34
43	...	53.068874	-27.879723	2.23	0.41	0.852	0.54	2.78	3.25	...	0.671
44	...	53.087166	-27.840195	2.21	0.12	1.80	0.32	0.869	1.69	...	[5.33]
45	195	53.041084	-27.837721	2.43	0.21	8.58	0.41	35.2	2.57	...	[3.09]
46	449	53.104912	-27.705305	2.29	0.11	250.	0.72	273.	4.68	1.613	1.69
47	739	53.163540	-27.890556	2.05	0.15	2.24	0.57	31.5	3.72	...	2.19
48	718	53.160664	-27.776251	2.04	0.36	3.08	0.34	1.34	1.73	2.543	2.58
49	234	53.053669	-27.869278	1.98	0.23	6.74	0.51	1.38	3.10	...	1.87
50	...	53.089542	-27.711666	1.97	0.45	1.16	0.66	-3.66	4.38	...	1.69
51	...	53.067833	-27.728889	1.94	0.22	0.793	0.55	6.95	3.54	...	2.32
52	...	53.064793	-27.862638	1.88	0.24	1.48	0.42	0.481	2.42	...	[3.63]
53	854	53.198875	-27.843945	1.86	0.32	5.19	0.45	124.	2.85	...	1.56
54	802	53.181995	-27.814196	1.82	0.30	-1.58	0.36	7.94	1.93	...	[1.85]
55	...	53.048378	-27.770306	1.79	0.15	0.720	0.48	1.41	2.58	...	[2.76]
56	458	53.107044	-27.718334	1.61	0.25	116.	0.54	391.	3.55	2.299	[2.93]
57	...	53.033127	-27.816778	1.72	0.26	0.738	0.41	0.879	2.62	...	3.08
58	...	53.183666	-27.836500	1.72	0.31	-0.191	0.37	-1.81	2.16
59	401	53.094044	-27.804195	1.84	0.13	2.04	0.35	46.2	1.78	2.325	1.24
60	...	53.124584	-27.893305	1.61	0.25	0.363	0.54	-0.257	3.27	...	2.53
61	...	53.132751	-27.720278	1.61	0.25	1.89	0.53	2.28	3.29
62	...	53.080669	-27.720861	1.59	0.17	2.67	0.57	-1.06	3.61	...	2.94
63	...	53.120041	-27.808277	1.57	0.26	1.41	0.29	1.08	1.64	...	1.83
64	...	53.117085	-27.874918	1.53	0.31	1.54	0.38	3.76	2.28	...	3.26
65	588	53.131458	-27.841389	1.46	0.14	1.09	0.29	13.6	1.66	...	1.58
66	203	53.044708	-27.802027	1.44	0.26	1.76	0.37	6.95	2.13	0.653	0.680
67	310	53.072002	-27.819000	1.36	0.19	1.41	0.32	5.30	1.69	...	1.69
68	...	53.120461	-27.742083	1.35	0.24	.00277	0.41	2.69	2.21
69	...	53.113125	-27.886639	1.25	0.27	0.477	0.46	1.84	2.84	...	2.55
70	...	53.141251	-27.872860	1.18	0.25	0.0897	0.39	5.38	2.29	...	3.14

Table 2 continued

Table 2 (*continued*)

C18 No.	L17 No.	R.A. J2000.0 (3)	Decl. J2000.0 (4)	$f_{850\,\mu m}$ (mJy) (5)	Error (6)	$f_{0.5-2\,\text{keV}}$ ($10^{-17}\,\text{erg cm}^{-2}\,\text{s}^{-1}$) (7)	Error (8)	$f_{2-7\,\text{keV}}$ ($10^{-17}\,\text{erg cm}^{-2}\,\text{s}^{-1}$) (9)	Error (10)	z_{spec} (11)	z_{phot} (12)
71	245	53.056873	-27.798389	1.16	0.30	1.81	0.34	2.48	1.85	...	1.71
72	527	53.119957	-27.743137	1.11	0.29	3.46	0.38	-0.155	2.11
73	...	53.142872	-27.874084	1.07	0.17	1.10	0.41	2.38	2.37	...	2.19
74	395	53.093666	-27.826445	0.93	0.23	2.30	0.32	2.56	1.76	0.732	0.766
75	...	53.074837	-27.787111	0.84	0.14

NOTE—The columns are (1) ALMA source number from C18, (2) X-ray source number from L17 when match exists, (3) and (4) ALMA R.A. and Decl., (5) and (6) ALMA 850 μm flux and error from C18, (7) and (8) observed 0.5–2 keV flux and error, (9) and (10) observed 2–7 keV flux and error, (11) specz, and (12) photz from H14, or, if there is no photz in H14, then from S16. We provide a FIR-based redshift estimate from C18 in brackets if there is no specz or high-quality photz available.